DEVELOPMENT OF A VOLUMETRIC 3D PARTICLE TRACKING VELOCIMETRY SYSTEM AND ITS APPLICATION TO MIXING IN A STIRRED TANK

by

YE CHENG

A thesis submitted to the

Graduate School-New Brunswick

Rutgers, The State University of New Jersey

in partial fulfillment of the requirements

for the degree of

Master of Science

Graduate Program in Mechanical and Aerospace Engineering

written under the direction of

Professor Francisco Javier Diez

and approved by

_____

_____

_____

New Brunswick, New Jersey

January, 2009

ABSTRACT OF THE THESIS

Development of a Volumetric 3D Particle Tracking Velocimetry System and Its Application to Mixing in a Stirred Tank

By YE CHENG

Thesis Director:
Professor Francisco Javier Diez

Quantitative fluid flow visualization and measurements are highly demanded in mechanical, chemical, medical and many other science and engineering fields to investigate fluid phenomena, understand theoretical principles and support computational prediction. Three-dimensional Particle Tracking Velocimetry (3D-PTV) is a powerful and comprehensive measurement technique that provides instantaneous 3D volumetric velocity information and Lagrangian description of particle trajectories. This work is based on the 3D-PTV technique that was developed at the Institute of Geodesy and Photogrammetric at the Swiss Federal Institute of Technology, Zurich. Theoretical principles of the technique were studied based on geometric imaging and computer vision.

A complete 3D-PTV system was designed, assembled, synchronized, and tested. A study of the accuracy of the 3D-PTV system in terms of the influence of each component was performed. 2D-PIV (Particle Image Velocimetry) measurements were done on the same experimental setup used in the 3D-PTV system. Results showed good quantitative agreement between the velocity information obtained with the two systems, which validates the results of the 3D-PTV measurement system. The developed 3D PTV system was applied to the study of mixing in a stirred tank showing that this technique has great potential for the study of low Reynolds number flows where the time-resolved trajectory of particles is important. Further improvement on the configurations and data analysis of the system can provide higher accuracy, higher spatial and temporal resolution, and less complexity, which will lead to an extension on its application.

ACKNOWLEDGEMENT

I would like to show my gratitude to my advisor, Prof. F. Javier Diez, for his constant support, guidance, and encouragement throughout my Master's research and studies at Rutgers University. Not only did he teach me the basics of experimental fluid dynamics, he motivated me when I was discouraged, inspired me with his passion when I became frustrated and impressed me with his patience when I experienced setbacks. I would also like to thank Prof. Alberto Cuitino and Prof. Haym Benaroya for sitting on my thesis committee and sharing their time and valuable advice to improve this work.

Many thanks go to John Petrowski for his technical assistance and suggestions. I would especially like to thank my labmate, classmate and roommate, Maria Del Mar Torregrosa, for her help, ideas, and company. I also want to thank Kevin Washington for his assistance on this work, Mariusz Zarzecki for his practical suggestions, and all the other members of the Experimental Fluids Lab. Thanks to Megan E. Smith for proofreading my chapters, to Jingru Zhang for computing simulations of my fluid experiment, to Jianbo, Xiaoliang, Venkat, Cass, Alex, Tyree, Hatice, and all my friends at Rutgers for making my life and studies enjoyable.

I would like to acknowledge the 3D-PTV group at ETH Zurich for their open source on

their great research and their insightful and helpful advice on this work.

Last but not least, I would like to express my gratefulness to my family and all my friends for their love, care, and encouragement. Thank you to my dad Cheng, Yanping and my mom Wang, Chunxiang for leading me into the field of science and engineering, and for their endless love and support.

TABLE OF CONTENTS

LIST OF TABLES

LIST OF FIGURES

Chapter 1

Introduction

1.1 Motivation

Human beings have never stopped showing their curiosity for different fluid flow phenomena in the nature. The most common fluids around us are air and water, however, they are transparent, which means their motions are invisible to us. The original approach to flow measurement might have been when our ancients threw wood into the river to test how fast the water was moving. Today, we are still fascinated by the natural or artificial flow motions and we are seeking to advance quantitative flow measurement techniques. In modern fluid mechanics, the experimental method plays a vital role on the understanding of theoretical principles and supporting of computational prediction. The demand for more complete, accurate, and convenient flow measurement techniques is increasing rapidly. Different approaches have been made and the fast improvement of photographic, optical and computer technology makes higher temporal and spatial

resolution, higher accuracy, and more robust flow measurement systems possible. Three-dimensional Particle Tracking Velocimetry (3D-PTV) is a powerful and comprehensive technique proposed at ETH Zurich to provide instantaneous 3D volumetric velocity information and Lagrangian description of particle trajectories. The objective of this work is to design, setup, assemble, and investigate the influence of different components of the 3D-PTV system, to validate the system with conventional Particle Image Velocimetry (PIV), to apply it to a typical 3D volumetric flow in pharmaceutical mixing, to further develop the technique itself, and to explore its range of applicability.

1.2 Review of Flow Measurement Techniques

Many techniques have been developed for flow field diagnostic, including conventional intrusive method such as Pitot-static probe or thermal anemometry and non-intrusive optical method such as Particle Image Velocimetry (PIV). The intrusive methods provide velocity information only at the point where the sensor is placed and thus the spatial resolution is very limited. Also, the flow field is influenced by the probe itself as it is intrusive. Optical flow measurement techniques, on the other hand, are non-intrusive methods with higher spatial and temporal resolution that can provide velocity information together with visualization of the flow.

Particle Image Velocimetry (PIV) is a well accepted tool for velocity field diagnostic that

quantitatively measures the fluid velocity at a large number of points [1]. As the name suggests, PIV captures the movement of illuminated tracer particles seeded in the fluid using digital cameras. The configuration of an original single PIV system is shown in Fig. 1.1. [1] This figure shows a laser sheet is used to illuminate the particles seeded in the flow. The light scattered by the particles is then recorded with a CCD camera. Two images of the particles are taken very closely to each other and are then divided into small interrogation windows for cross-correlation. The two-dimensional velocity is then obtained for each interrogation window and the velocity field is generated for the flow.

As three-dimensional velocity measurement is demanded in many applications, single-PIV with only two-dimensional information is extended to stereo-PIV by introducing a second camera or with a hybrid stereoscopic camera [2]. The out-of-plane velocity component can be obtained by placing two cameras at different viewing angles, which causes a displacement in 2D images that can be interpreted into the third component velocity. Stereo-PIV tends to have lower accuracy on the out-of-plane velocity compared to the in-plane velocity components [3]. The accuracy of the velocity depends on the accuracy of reconstruction from 2D distorted images to 3D particle displacement, which is determined through a generalized calibration procedure [4]. Another approach was made by Raffel et al. (1996) to obtain the third component velocity, using a dual-plane PIV system with a second laser sheet parallel and slightly displaced from the original one [5]. Both methods create an improvement on the original single-camera PIV as they provide

the velocity information in three components and also help to eliminate prospective error.

With the development of photographic, laser, and data acquisition technology, the temporal resolution of optical flow measurements also increases. High-speed PIV systems are developed with the invention of high frame rate cameras and high repetition rate lasers. Commercial high-speed system from Dantec Dynamics A/S can reach a capture rate of 10 kHz [6]. A new time-resolved PIV system with a frame rate of 25 kHz has been applied to the study of hot Jet by NASA Glenn Research Center in 2007 [7].

Time-resolved PIV enables the possibility of instantaneous flow velocity measurement in a volume. Tomography was introduced into conventional PIV in the form of scanning-PIV. Fig. 1.2 illustrates the experimental setup of a time-resolved tomographic PIV system [11]. As shown in the figure, scanning-PIV extends the velocity in a plane into a volume by the capture of images in a series of parallel planes distributed along the third axis. A synchronized scanning mirror drum was used to create the multiple laser light sheets and a volume of 100mm x 100mm x 100mm with 3D vectors was presented by Guezennec et al. (1994) [8]. Ciofalo et al. (2003) combined two orthogonal families of parallel scanning planes with tomographic PIV system to obtain 3D volume flow field [9]. A recent work (Haan et al. 2008) applied the tomograhpic and time-resolved PIV system on the study of the flow over a cylinder stump with a spatial resolution of 3512 x 2562 x 599 voxel and temporal resolution of 1000 Hz [10].

Holographic PIV is another technique for 3D volume flow measurements. This technique measures the instantaneous 3D velocity field in a volume using holography. The 3D displacement of particles is recorded on a double exposure hologram instantaneously, and is then reconstructed to the 3D domain. The term holographic PIV was first introduced by Barnhart et al. (1994) and they were able to attain 400,000 3D vectors in a 24.5mm x 24.5mm x 60mm volume [12]. Both in-line and off-axis holographic PIV systems were compared and combined to maintain the simplicity of in-line perspective and the higher signal to noise ratio of off-axis perspective [13]. A more recent work by Sheng et al. (2003) introduced one-beam two-view holographic PIV, which increased the spatial resolution and remained the simplicity of using single recording system but recording two orthogonal views [14]. Holographic PIV provides a volumetric flow measurement and also eliminates the particle image overlap problem, but the complexity of the system and the time-consuming image reconstruct procedure are the obstacles on this technique.

Although the particle image velocimetry methods stated above can offer relatively high temporal and spatial resolution flow measurements of two-dimensional or three-dimensional in a plane or a volume, their results are restricted to vector fields only, instead of real particle trajectories. All different PIV techniques provide the Eulerian description of the flow field, which gives mean velocity of a group of particles at different spatial positions. However, Lagrangian description which follows individual

particles is also demanded in many applications. Particle Tracking Velocimetry (PTV) is the flow measurement technique that identifies individual tracer particle displacements based on Lagrangian description. The advantage of PTV over PIV is that while PIV provides statistical displacement of group of particles rather than individual ones, PTV provides truly local velocity information for individual particles, but this leads to the drawback of difficulty on correspondence determination at different time steps. Also, flow measurement is restricted to low seeding concentration flows. Many PTV systems have been developed to overcome the cost of lower spatial resolution. Hassan et al. (1991) introduced a four-frame particle tracking method which traced the particles frame by frame by searching the neighborhoods based on the consistency of the particle displacement [15]. A neural-network PTV algorithm was proposed by Labonté (1999) to eliminate the correspondence problem of particle identification. The technique was based on two-frame tracking which sought for matching particles by approximately duplicating the flow motion [16].

Three-dimensional Particle Tracking Velocimetry (3D PTV) is a more recent and comprehensive flow measurement technique that follows individual particles in a volume within many time steps and provides particle 3D positions and velocities. This technique was first proposed by the Institute of Geodesy and Photogrammetry, the Institute of Hydromechanics and Water Resources Management at the Swiss Federal Institute of Technology in 1989 [17]. The 3D-PTV system is based on the acquisition and processing

of a sequence of tracer particle images from several cameras at different orientations [18] [19]. The system was able to investigate the flow in a volume of size up to 200mm x 150mm x 50mm and with particle trajectories up to 1000 at temporal resolution of 25Hz [20].

Another notable 3D volume flow measurement technique is called Defocusing Digital Particle Image Velocimetry (DDPIV). The principle was first brought up by Willert et al. (1992) [21]. They used three pinhole apertures shifted away from the optical centerline forming an equilateral triangle, and with the three image spots left by the same particle, the relative position of each particle to the reference plane could be recovered from the orientation of the triangle. This technique was able to investigate the bubble flows within a cubic foot volume [22]. DDPIV can provide individual particle positions in a considerably large volume, but it requires very high intensity of illumination, is limited to the study of relatively large (several hundred microns) tracer particle and is subjected to low spatial resolutions due to required low seeding concentrations.

After the comparison of a wide range of flow measurement techniques from conventional intrusive Pitot probe, anemometry, to classical optical technique 2D single PIV, to three-component stereo-PIV, and to the different approaches on 3D volumetric whole-field measurement such as holographic PIV or defocusing PIV, 3D-PTV proves its great potential on the diagnostic of large volumetric flow seeded with tracer particles of

different size ranges providing long trajectories over time.

1.3 Thesis Outline

Chapter 2 gives a brief description of the mathematical theory inside 3D-PTV techniques. Two different flow description perspectives are compared and the projective algorithm from 3D world to 2D images is explained together with the mathematical principle of identification of the same particle in different camera views. Chapter 3 details the experimental setup of the 3D-PTV system, describes different components separately and the connection between them. Chapter 4 describes the data acquisition procedure and analysis process for a complete 3D-PTV measurement and result presenting with step by step calibration procedure and image analysis flow charts. Chapter 5 goes in depth and breaks down the 3D-PTV system into different components to study their influence on the reliability and accuracy of the whole system separately. Preliminary results of the system testing on a simple flow are presented. Chapter 6 demonstrates the validation of the 3D-PTV technique with a conventional single PIV system under the same experimental condition. The PIV system and the object flow are described and the comparison of both methods is presented. Chapter 7 presents the application of 3D-PTV technique on the study of pharmaceutical mixing. Results of 3D particle trajectories, 3D volume vector fields, and the comparison with different mixing speeds, different locations, and different particle sizes are illustrated. Chapter 8 is the conclusion remarks

and suggestion for future works on the 3D-PTV technique.

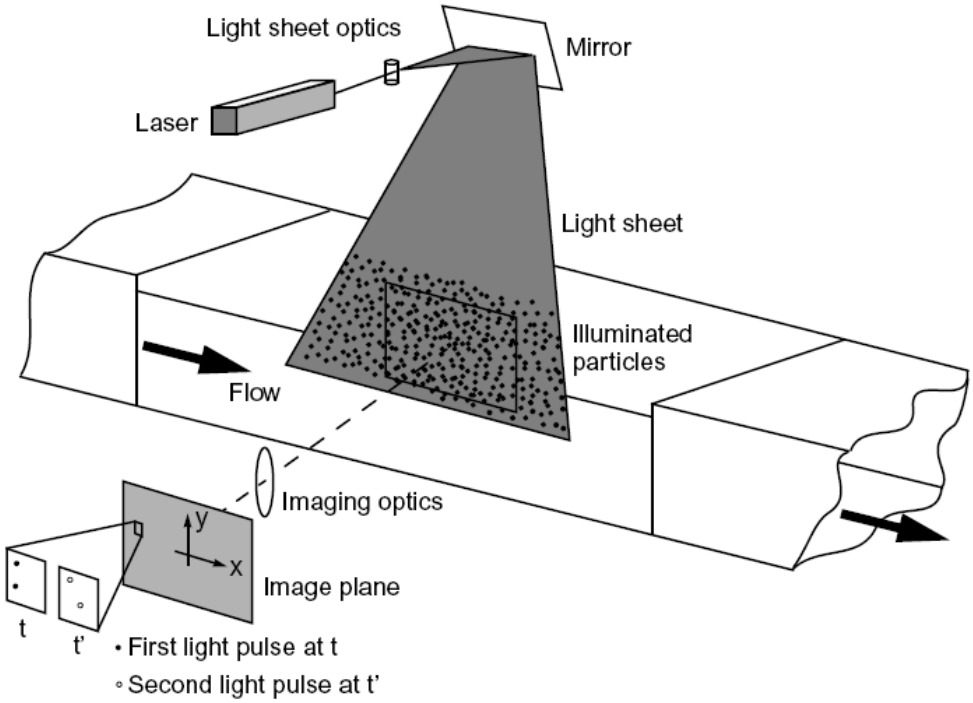

Figure 1.1. Typical configuration of a Particle Image Velocimetry system in a wind tunnel. (Raffel et al. 1998)

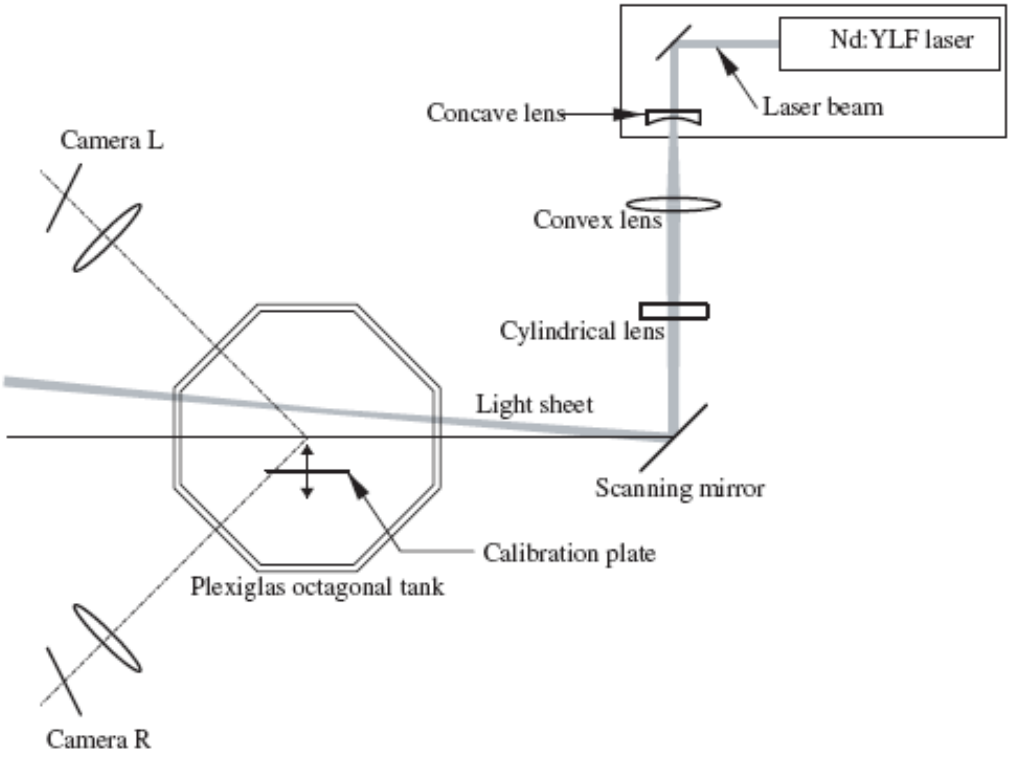

Figure 1.2. Optical configuration of a scanning stereoscopic PIV system (Hori et al. 2004)

Chapter 2

3D-PTV Reconstruction Geometry

In this chapter, the mathematical algorithm and geometry theory of 3D-PTV system is discussed. 3D-PTV is based on descriptions of flow movement (time correlation), as well as transformation between image plane and object volume, and establishment of correspondence between multiple cameras (spatial correlation).

2.1 Eulerian Description and Lagrangian Description

For the description of a flow field, there are two different points of view: Eulerian and Lagrangian. An Eulerian description describes the motion as a function of both space and time, and is mathematically expressed as:

$$\vec{u} = \vec{u}(\vec{x}, t)\,. \tag{2.1}$$

The Eulerian description defines a velocity field based on fixed points in space between different time steps, as shown in Fig. 2.1a. A Lagrangian description tracks individual particles through the velocity field and gives the trajectories of these individual particles

as a function of time, as shown in Fig. 2.1b. The trajectory, also called the pathline, is the actual path traversed by an individual fluid particle [23]. The position, velocity, and acceleration of each particle can also be obtained through this description [24].

For flow visualization, most experimental techniques provide the Eulerian description of the flow (e.g. Particle Image Velocimetry (PIV) and Laser Doppler Velocimetry (LDV)). Particle Tracking Velocimetry (PTV), in the other hand, is based on a Lagrangian description of the velocity field and, with a relatively low-concentration seeded flow, the movement is tracked according to each individual particle.

2.2 Single Camera Geometric Imaging

3D-PTV is a powerful flow visualization technique that is able to locate the 3D position of individual particles based on multiple 2D images taken by cameras with different perspectives. Particle identification between images taken from different cameras is used and the particle position is converted between the two-dimensional image plane and the three-dimensional world coordinate system.

The simplest case of camera geometry is the correlation between object and image for a pinhole camera, as shown in Fig. 2.2. The light reflected from the object point P, passes through the small aperture pinhole of the camera and forms an image point P', on the

camera image plane. If the object P is a 3D object (instead of a point), then the image P', becomes a 2D projected shape. This occurrence is called perspective projection, which is defined as the projection of a three-dimensional object onto a two-dimensional surface by straight lines that pass through a single point [25]. The single point is called the projection center, and is labeled as C in Fig. 2.2. Fig. 2.2 shows the two coordinate systems involved in the projection of the object from world coordinates to image coordinates. These are the 3D world coordinate system (X, Y, Z) and the 2D image coordinate system (x, y). In the world coordinates, the object point, P, is (X_o, Y_o, Z_o), and the projection center, C, is (X_c, Y_c, Z_c). In the image coordinates, the image point P', is (x_i, y_i). To make the coordinate conversion, homogeneous coordinates are commonly used [27]. The homogeneous coordinates linearize the non-linear perspective projection equations by mapping each point (X, Y, Z) in three-dimensional space onto a line that passes through the origin in four-dimensional space [25]. In this case, the physical object point P (X_o, Y_o, Z_o) in 3D space is represented by a 4×1 vector in homogenous coordinates by introducing a nonzero and arbitrary constant w, as follows:

$$\begin{pmatrix} X_O \\ Y_O \\ Z_O \end{pmatrix} \rightarrow \begin{pmatrix} wX_O \\ wY_O \\ wZ_O \\ w \end{pmatrix}, \qquad \textbf{(2.2)}$$

where $w \neq 0$.

The perspective projection from the physical object point P (X_o, Y_o, Z_o) to the image point P' (x_i, y_i) then becomes:

$$\begin{pmatrix} w_i x_i \\ w_i y_i \\ w_i \end{pmatrix} = \begin{bmatrix} a_{11} & a_{12} & a_{13} & a_{14} \\ a_{21} & a_{22} & a_{23} & a_{24} \\ a_{31} & a_{32} & a_{33} & a_{34} \end{bmatrix} \begin{pmatrix} X_o \\ Y_o \\ Z_o \\ 1 \end{pmatrix}. \quad \textbf{(2.3)}$$

The equation can be rewritten as:

$$x_i = \frac{w_i x_i}{w_i} = \frac{a_{11}X_o + a_{12}Y_o + a_{13}Z_o + a_{14}}{a_{31}X_o + a_{32}Y_o + a_{33}Z_o + a_{34}},$$

$$y_i = \frac{w_i y_i}{w_i} = \frac{a_{21}X_o + a_{22}Y_o + a_{23}Z_o + a_{24}}{a_{31}X_o + a_{32}Y_o + a_{33}Z_o + a_{34}}. \quad \textbf{(2.4)}$$

The coefficients a_{ij} in the 3×4 conversion matrix are nonlinear functions of the camera focal length f, camera projection center position X_c, Y_c, Z_c, camera body rotation angles θ_X, θ_Y, θ_Z, and other lens distortion and decentering distortion parameters [26]. These unknown coefficients can be obtained from calibration process, which uses a series of known-position dots as the reference. Given one object point and image point pair (P (X_o, Y_o, Z_o) and P' (x_i, y_i)), two equations are established. There are twelve unknowns in the conversion matrix, and thus at least six known point pairs are needed [27]. Description of the calibration process is presented in Chapter 4.

2.3 Multi-Camera Geometric Imaging and Correspondence

When applying 3D reconstruction from 2D images, the image point position in the image coordinates (x_i, y_i) is a known variable, while the real position of the object (X_o, Y_o, Z_o) is unknown. The solution is not unique, as there are three unknowns and only two equations with a single camera configuration. For this reason, a second camera with a

different perspective is necessary for 2D to 3D reconstruction.

Two cameras looking at the same object from two different perspective creates a pair of stereo images. The z component of the three dimensional position can be reconstructed from the disparity of a stereo pair of image points [28]. However, the recognition of a stereo pair of image points becomes a problem, as there can be multiple ambiguities. A stereo camera system is shown in Fig. 2.3. The sketch in this figure show how an image point P_1 in camera 1 can be recovered into object points, , at any point along the C_1P_1 line such as P_a, P_b, or P_c. Thus in camera 2, the corresponding half of the stereo pair could be P_{2a}, P_{2b}, P_{2c}. The fact that all the possible halves of the stereo pair are located along a straight line is called epipolar geometry and the line, shown as $P_{2a}E_{c2c1}$, is called the epipolar line. For simplicity, the epipolar line in camera 1 is named as e_{21}, and the one in camera 2 as e_{12}. E_{c2c1} is found by connecting two camera projection centers C_1 and C_2 together, and the intersection of C_1C_2 and the second camera image plane is E_{c2c1}, known as the epipole. The issue of correspondence is a very significant problem found in 3D-PTV, due to the large depth of laser light volume and the relatively high concentration of tracer particles. Particle correspondence between four cameras refers to the process of identifying the image points of the same actual particle in different camera images.

An evaluation of the number of possible image points in the second camera was discussed by Maas (1992) [29]. Fig. 2.4 illustrates the top view of the two-camera system

geometry. Given an image point in camera 1 P_1', the possible object point can be anywhere between P_1P_2 within the laser sheet. The actual corresponding half of image point P_1' in camera 2 is called P_2', and can be found between x_1'' and x_2''. This distance is called the length of the epipolar search window (l_{12}) and can be derived from simple geometry in the following format:

$$\begin{aligned} l_{12} &= x_1'' - x_2'' \\ &= f \times \left(\frac{b_{12} - X_1}{Z_{\min}} - \frac{b_{12} - X_2}{Z_{\max}} \right) \\ &= f \times \left(\frac{b_{12}}{Z_{\min}} - \frac{b_{12}}{Z_{\max}} \right) \\ &= \frac{f \times b_{12} \times (Z_{\max} - Z_{\min})}{Z_{\max} \times Z_{\min}} \end{aligned}, \quad \textbf{(2.5)}$$

where f = focal length of the camera and b_{12} = the distance between the two cameras. Within this distance in camera 2, there exist many possible candidates for each stereo pair of image points. For an entire image full of particles, the total number of possible candidates in camera 2 is:

$$N = n \times (n-1) \times \frac{2 \times l_{12} \times \varepsilon}{F}, \quad \textbf{(2.6)}$$

where n = total number of particles per image and ε = tolerance width.

To decrease the number of ambiguities, a third camera is introduced into the system. As shown in Fig. 2.5, the correspondence of an arbitrary image point P_1 in the first camera, can be found along the epipolar line e_{12}, in the second camera identified by, for example, P_{2a}, P_{2b}, and P_{3c}. The three candidates produce three epipolar lines e_{23a}, e_{23b}, and e_{23c} in

the third camera, while P_1 produces an epipolar line e_{13} in the third camera. The correspondence can be found by looking for the intersection between e_{23a}, e_{23b}, e_{23c} and e_{13}, where a triplet is identified. The third camera can decrease the number of possible candidates by a factor of 10 [29], but there are still ambiguities that make the correspondence non-unique.

The introduction of a fourth camera can further decrease the number of candidates. Fig. 2.6 shows the intersection of epipolar lines between four cameras. By applying the epipolar lines from camera 1 to camera 2 (e_{12}), four ambiguities are found in camera 2. The intersection between epipolar line e_{13} and e_{23} in camera 3 decreases the number of ambiguities to two. Finally the intersection between epipolar line e_{14} and e_{34} in camera 4 further reduces the number of ambiguities and identifies the actual corresponding points in the four cameras, known as a set of quadruplet. By using the forth camera, the number of ambiguities can be reduced by a factor of 100, as compared to the stereo setup, and the uniqueness of the quadruplets is almost achieved. More cameras can be used in the system, but they are not necessary, as significant improvement is not accomplished.

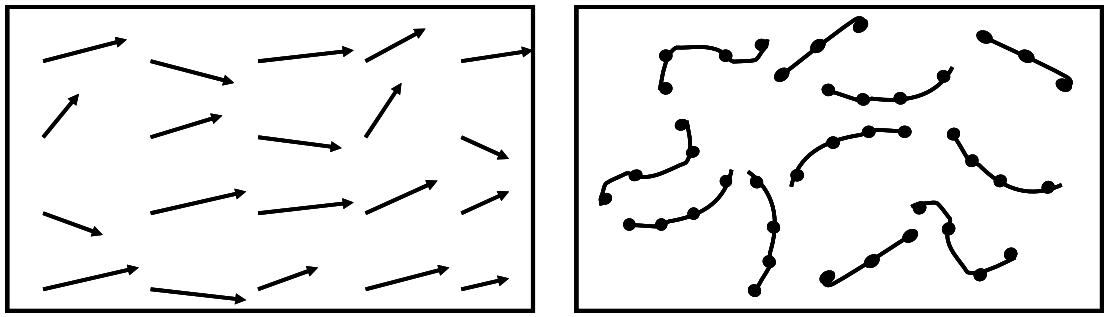

a) Eulerian Description-->Vector Field **b) Lagrangian Description-->Trajectories**

Figure 2.1. Eulerian and Lagrangian description

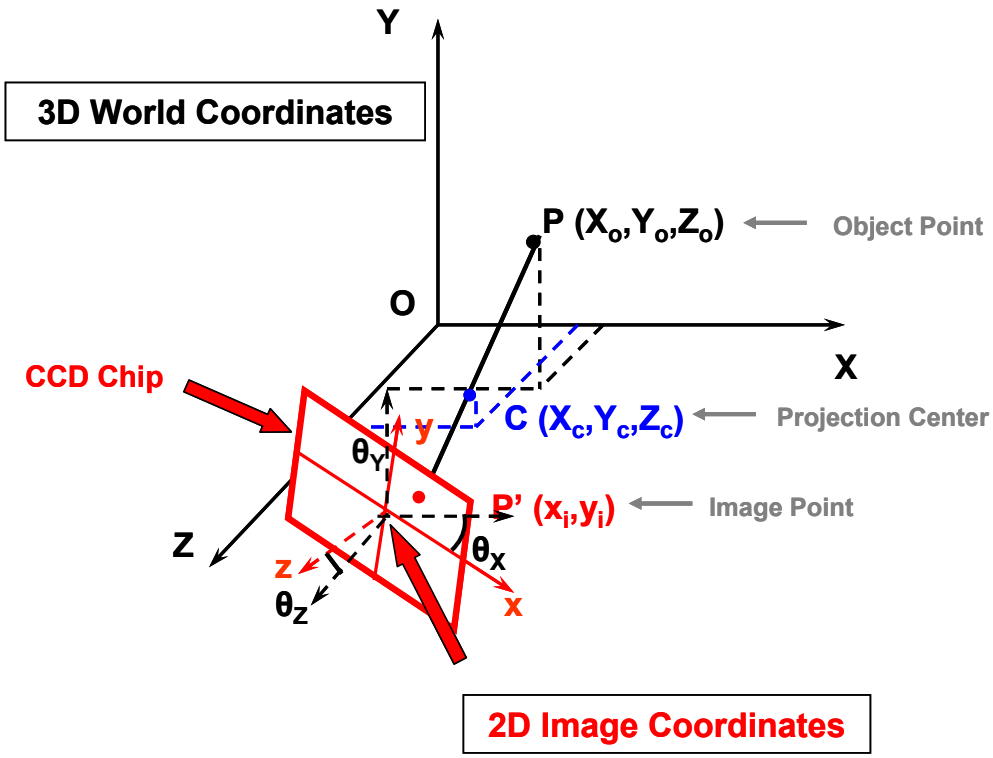

Figure 2.2. Schematic representation of geometric imaging for one camera
Black frame: 3D world coordinate system (X, Y, Z)
Red frame: 2D image coordinate system (x, y)
Camera body rotation angles: θ_X, θ_Y, θ_Z

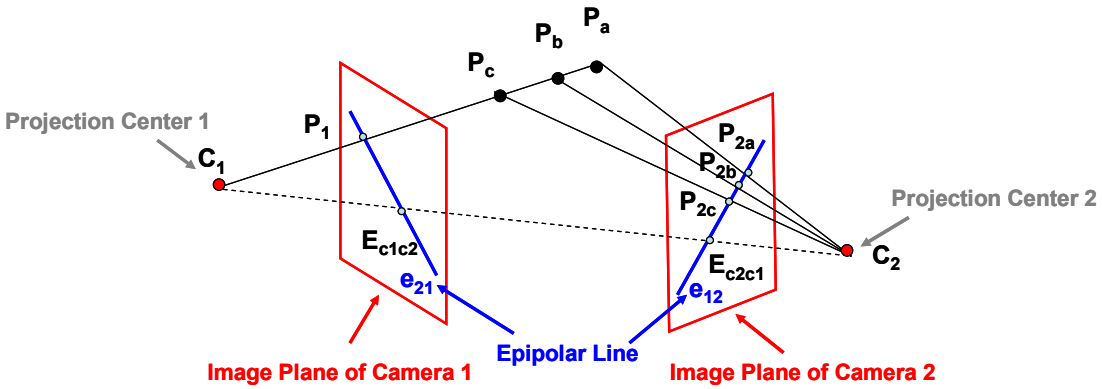

Figure 2.3. Schematic representation of geometric imaging for two cameras (Epipolar geometry)
Epipolar lines: from camera 1 to camera 2 (e_{21}); from camera 2 to camera 1 (e_{12})

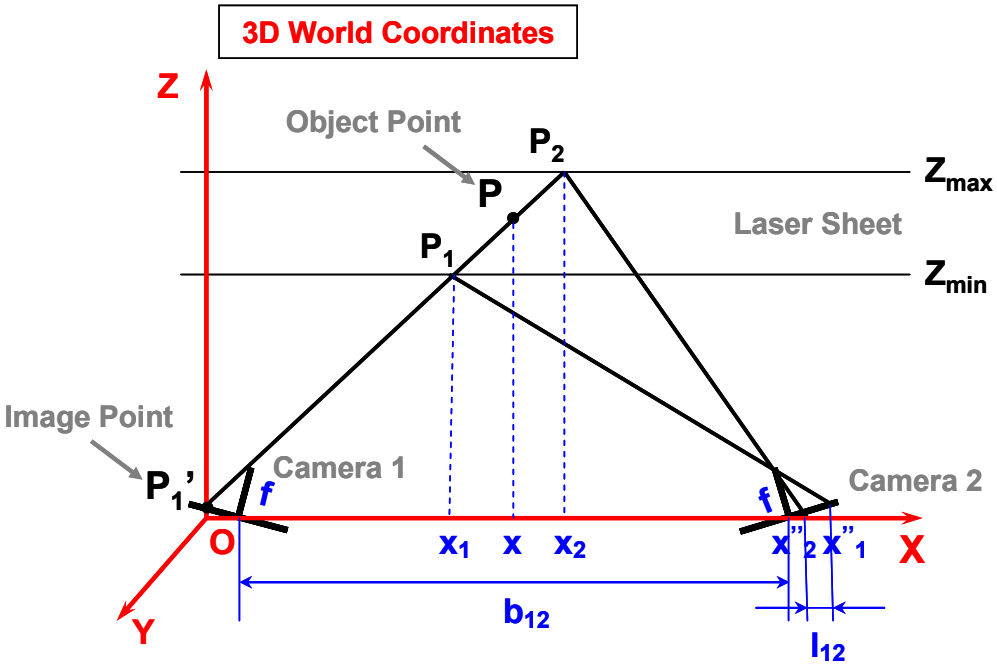

Figure 2.4. Correspondence in 3D-PTV
(Epipolar geometry in particle identification between two camera images)

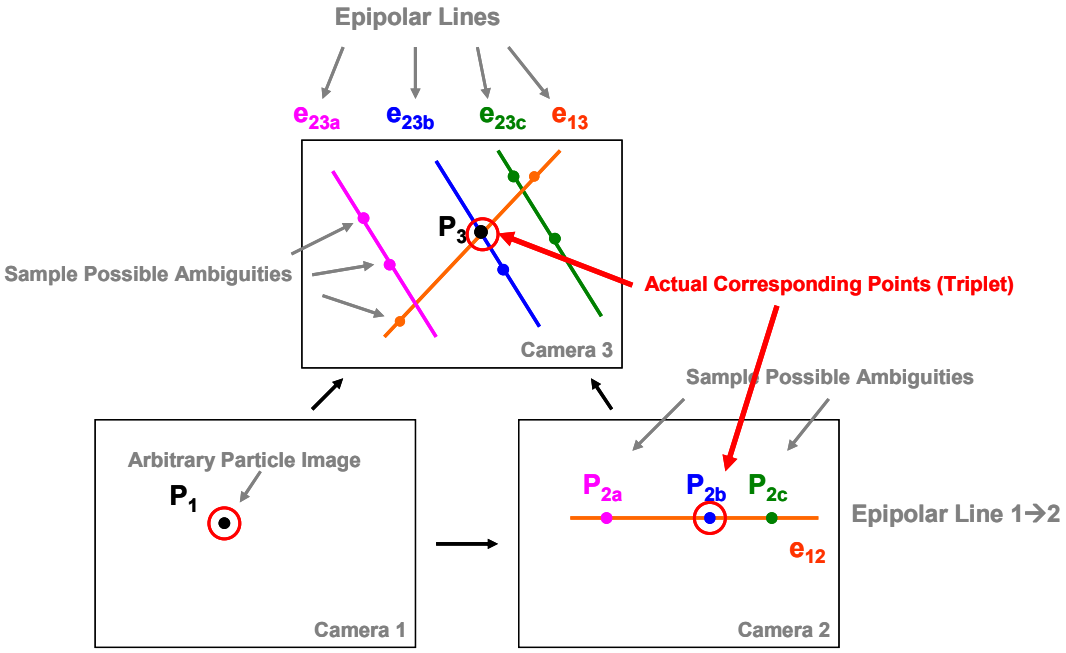

Figure 2.5. Three camera correspondence

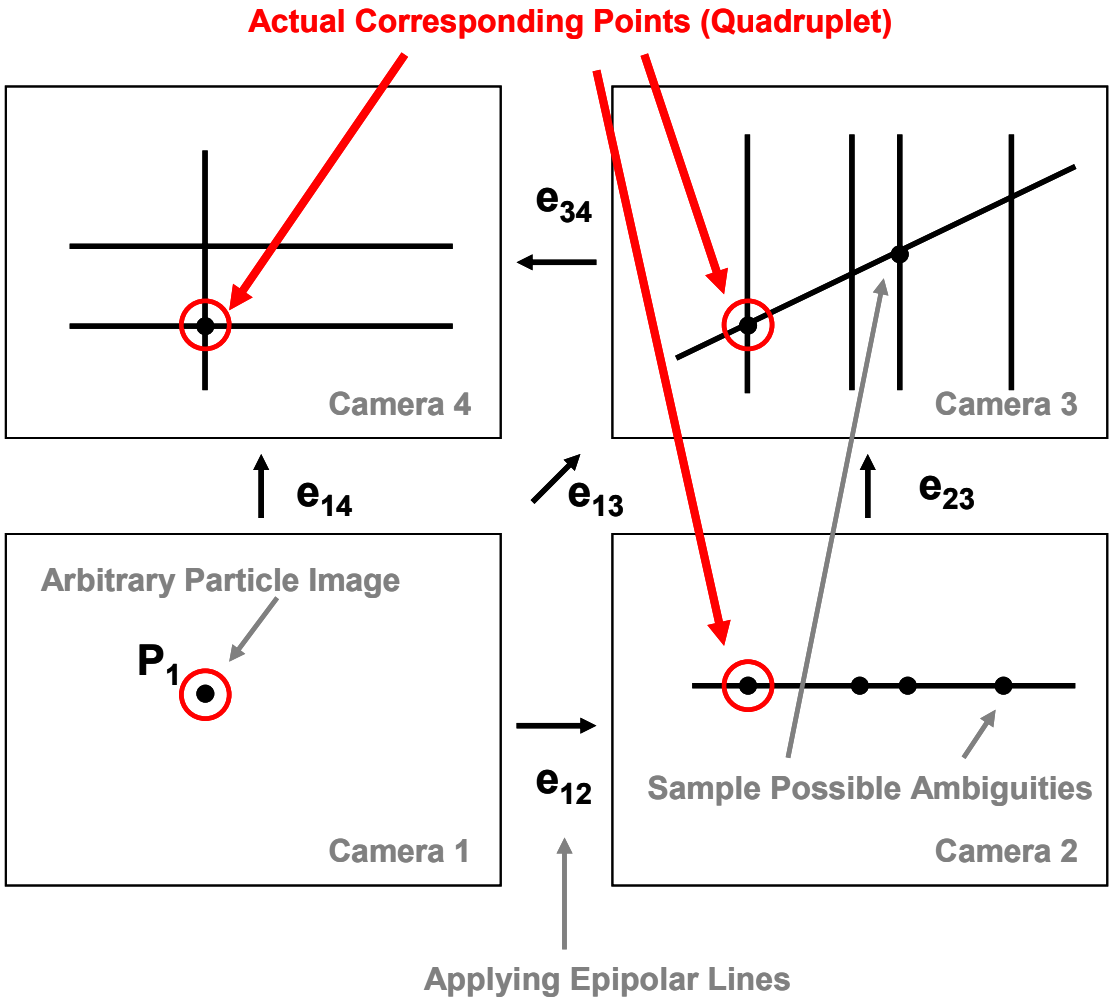

Figure 2.6. Four camera correspondence

Chapter 3

3D-PTV Experimental Setup

In this chapter, the hardware configuration and timing synchronization of the 3D-PTV system are discussed. To visualize the flow, a synchronized image acquisition system is developed to capture the positions of the tracer particles illuminated by a laser light source. The following components of the system will be discussed: the image acquisition system, system synchronization, laser illumination volume, tracer particles, and calibration target.

3.1 Image Acquisition System

The image acquisition system consists of four charge-coupled device (CCD) cameras, two synchronizers, four frame grabbers, two computers, one Nd: YAG laser, and an optical fiber or cylindrical lenses. As shown in Fig. 3.1, the laser light exits from the optical fiber and forms a light cone to illuminate the tracer particles in the fluid. Four

cameras are placed and focused onto the same region of the illuminated volume. This is known as the observation volume. The four cameras are separated into two pairs for the purpose of synchronization. Each pair of cameras is connected to a synchronizer (digital delay generator) and then to a computer for image acquisition. The master synchronizer sends a signal that triggers the slave synchronizer. The outputs of the system are sets of four particle images from four cameras each with a different perspective.

The cameras used in the system are double exposure Kodak MegaPlus ES 1.0, with capture rate of 15 frame/s, image resolution of 1008 x 1024 pixels, and an active CCD sensor area of 9.1mm x 9.2mm. The four camera lenses are Nikon 50mm f/1.8 AF lenses. The four cameras are mounted on three degrees of freedom mounts with a nearly square configuration. A snapshot of the camera configuration is shown in Fig. 3.2.

Two PCs loaded with TSI IINSIGHT 3G Software are used to capture and store the images. The INSIGHT3G Global Image Acquisition, Analysis, and Display Software was introduced in 2004 by TSI, Inc. It is a Microsoft Windows XP-based software that is used for global image capture, analysis, and display purposes. In the present 3D-PTV application, the software serves as an image acquisition interface and, thus, only the image capture function is used.

Each of the computers was connected to a TSI 610034 LASERPULSE Synchronizer,

which acts as a master timing unit between cameras, frame grabbers, laser flash lamp, and Q-switch. As shown in Fig. 3.1, each synchronizer was connected to two cameras, and the dual head laser was connected to one of the synchronizers. The detailed system synchronization is explained in Section 3.2.

A New Wave Solo PIV Nd: YAG Laser system was used to illuminate the observation volume. The laser has a repetition rate of 15Hz, energy of 15mJ at 532nm wavelength, and a beam diameter of 5mm. The beam was delivered and expanded into a uniform light volume using a Newport Liquid Light Guide.

3.2 System Timing and Synchronization

As explained in Chapter 2, a four-camera configuration for 3D-PTV enables the reliable identification of valid particles by searching for the intersection of epipolar lines. However, the reliability is highly dependant upon the system synchronization. Four CCD cameras must be exposed simultaneously, when the laser fires. This synchronization is crucial as any time delay between the four cameras will cause the correlation between the four particle images to be subjected to flow movement.

Fig. 3.1 shows the camera setup with camera I and II connected to synchronizer I and to PC I, and camera III and IV connected to synchronizer II and PC II. The dual head laser

is connected to synchronizer I. Fig. 3.3 indicates the timing setup for the 3D-PTV system. Both synchronizers simultaneously generate a square wave rising edge which starts the exposure time of the cameras. After the mechanical shutters are open, the cameras send a feedback signal to the synchronizer. Then the synchronizer sends two TTL pulses to the laser: the TTL pulse triggers the flashlamp and the second TTL pulse triggers the Q-switch and the laser fires. The time between the firing of laser and the first synchronizer signal rising edge is called the laser pulse delay and needs to be less than the total camera exposure time. The camera shutters close at the end of the exposure time (281μs), which is the default value for the Kodak MegaPlus camera. A capture period is then completed. The capture frequency used in this system is 15Hz, which means that each camera captures 15 images per second.

To synchronize the four cameras, two different approaches were tested and proved to be reliable. The first method involves the use of an external trigger to start both synchronizers. A signal generator was used to generate a square wave function (0-5V), with a desired frequency of 15Hz. The signal was sent to both synchronizers, which operates as external triggers. When both capture functions are enabled through the software, both synchronizers wait for the external signal rising edge of 5V to generate the first pulse. Once the signal generator is started by the user, it will continue giving a square wave signal at 15Hz. Thus, both systems start simultaneously and continue to capture images at the frequency of the signal generator.

The second method used for synchronizing the four cameras required one synchronizer to trigger the second synchronizer (Master-Slave configuration). Fig. 3.4 illustrates the timing relationship between all the components. The laser was connected to one of the synchronizers, named synchronizer I, while synchronizer II was only connected to the other two cameras not to the laser. The camera trigger signal from synchronizer I served as the external trigger for synchronizer II. As shown in Fig. 3.4, when synchronizer I generates a signal to start the two cameras connected to it, the same signal was also sent to synchronizer II as an external trigger, so that synchronizer II generates a signal to start the two cameras connected to it. Thus, the four cameras have their shutters opened simultaneously, while the laser pulses during their exposure time. The four images are captured simultaneously when the laser fires.

Both methods of synchronization were tested by observing the signals of all the channels from both synchronizers on an oscilloscope, and were also tested by taking images of a digital stop watch. Both methods of synchronization are proved to be accurate enough at a frequency of 15Hz. The first method requires more wiring and hardware as well as a manual start. In addition, the accuracy of this method is dependent on the signal generator, but does have the advantage of having no time delay between the two sets of cameras. The second method is less complex, but the triggering between synchronizers creates a time delay of 30μs. At the low frequency of 15Hz (with a period of 66667μs),

this delay represents only 0.04% and is considered negligible. The second method of synchronization was applied in this work.

3.3 Laser Light Volume Illumination

To visualize the flow motion of a clear fluid (e.g. air or water), passive tracer particles are added to track the motion of the fluid. A high intensity and homogenous light source is required to illuminate the tracer particles so that their scattered light can be detected by the CCD cameras.

In this work, a double pulsed Nd: YAG laser is used operating at 532nm wavelength (visible green light). The Nd: YAG laser is optically pumped using a flashlamp. The pulsed Nd: YAG laser is operated by the Q-switch, which produces 3-5ns light pulses with extremely high peak power up to 120mJ. Also, the pulse duration is very short in order to 'freeze' the particle motion at one time step.

For the 3D-PTV application, an evenly illuminated light volume is desired. Fig. 3.5 shows a snapshot of a typical laser light volume illumination for 3D-PTV. The green area in the tank is produced by high power laser light illumination and shows the 3D-PTV observation volume.

Two approaches were taken in order to illuminate the measurement volume. In the first method, shown in Fig. 3.6, two concave cylindrical lenses of 15mm focal length and 25mm focal length were placed with optical axis orthogonal to each other. The 3mm diameter laser beam passes through the first cylindrical lens and expands into a laser sheet in vertical direction. Then the laser sheet passes through the second lens and is expanded in the horizontal direction to generate the desired volume. The distance between the plano-surface of the two lenses was set as the difference of the two focal lengths in order to decrease the beam divergence.

The second method to generate a light volume using a laser source is to use a liquid light guide. In this work, a Newport Liquid Light Guide with a 5mm core diameter and 2m length is used. The liquid light guide carries light by total internal reflection from the inner surface of the fiber. The laser light bounces back and forth in the fiber core and exits with a more homogeneous profile but higher divergence. The outlet of the fiber is placed at a certain distance from the observation area in order to get the desired volume size. The light volume is then changed from a cylinder to a cube by placing several black blocks along the edges of the light.

Both methods for generating a laser light volume illumination were tested. When comparing both methods, the volume created by the two cylindrical lenses is less affected by laser beam divergence problem. However, the cylindrical lenses expand the uneven

beam profile of the laser light, leaving fringe-like patterns throughout the entire illumination volume. In contrast, using the laser light guide produces a homogeneous light volume with even intensity, but the dimensions of the volume are influenced by higher beam divergence. For a 60mm x 60mm x 60mm volume, the cross section diameter difference between the upstream and downstream of the light was found to be 0.3cm, which is a 5% divergence. For application the present work, a more homogeneous light intensity is preferred rather than smaller beam divergence, and thus the liquid light guide was used for the final 3D-PTV system.

3.4 Tracer Particles

Tracer particles are neutrally buoyant, micron-size spheres that are seeded into fluid to follow the flow motions [1]. Fig. 3.7 shows two types of tracer particles observed through an optical microscope. The image on the left shows aluminum oxide particles, which have higher density but large particle size distribution. The silver coated ceramic particles in the right picture have better controlled size distribution and more even shapes.

As the flow motion measurement is based on imaging of scatter light by particles at two different instants, the quality of the particle is crucial to the reliability of the system. The tracer particles basically need to meet the following criteria: First, they need to have very similar density as the working fluid to be able to follow the flow motion. Second, they

need to have high light scattering ability to make them detectable in the images. Third, the size of the particles needs to be small enough to represent the flow motion, but also big enough to scatter adequate amount of light. Also, the shape of the particles is preferred to be even and spherical for light scattering and particle identification purpose. Some typical tracer particles used in water are polystyrene of 10-100μm diameter, aluminum flakes of 2-7μm diameter, hollow glass spheres of 10-100μm diameter, and oil drops or oxygen bubbles [1]. The choice of tracer particles highly contributes to the accuracy and reliability of the 3D-PTV experiments. Tests of different type of tracer particles are detailed in Section 5.3.

3.5 Calibration Target

To locate the particle 3D positions in the observation volume from the four images taken with four cameras, a conversion algorithm between the image coordinate system and world coordinate system is needed. The conversion is obtained from the calibration procedure by introducing an object with dots of known positions known as a 3D calibration target, as shown in Fig. 3.8. By taking a set of four images with four cameras at different positions from the reference object, a conversion can be established between the two different coordinate systems described in sections 2.2-2.3. This makes the calibration target another critical component of the 3D-PTV system. Fig. 3.8a shows the design of the target drawn with CAD software Pro-Engineering. Figure 3.8b shows the

final product of the calibration target.

The shape and dimension of the calibration target and spacing between reference dots are determined based on the experiment conditions. The design needs to follow several basic rules. First, the dimension of the target needs to match the dimension of the observation volume. If the target is too small, only part of the observation volume will be calibrated and the accuracy will decrease. Second, the reference dots on the target need to be evenly spaced in three directions. The spacing between the dots needs to be small enough to insure calibration precision. On the other hand, if the dots are too closely located, the number of calibration points per image is too high. This will complicate and slow down the calibration process and is not necessary. Third, the size of the reference dots needs to be big enough for the cameras to see them, but small enough to ensure the accurate identification of the center location. Also, the shape of the dots is preferred to be round as it helps to locate the center of the dots.

From a manufacturing perspective, the reference dots need to be precisely located at the designed positions. The shape of the dots needs to be homogeneous. High color contrast is required between the target body and the dots. Thus, a black target with white reference dots on it is a good choice. The final target used in the system was manufactured in an aluminum block by using Computer Numerical Control (CNC) machining. As shown in Fig. 3.8, the dimension of the target is 100mm x 70mm x 30mm, with 70 reference dots

on it. The spacing between the dots is 10mm. The dots were machined as small round concaves of 1.2mm diameter and 0.5mm depth. The calibration target body was then painted black. White epoxy was used to fill in the dot concaves. A white cross, the fulcrum, was marked at the center of the target as a reference. The influence of the calibration target in the accuracy of the system is further discussed in Section 5.1.

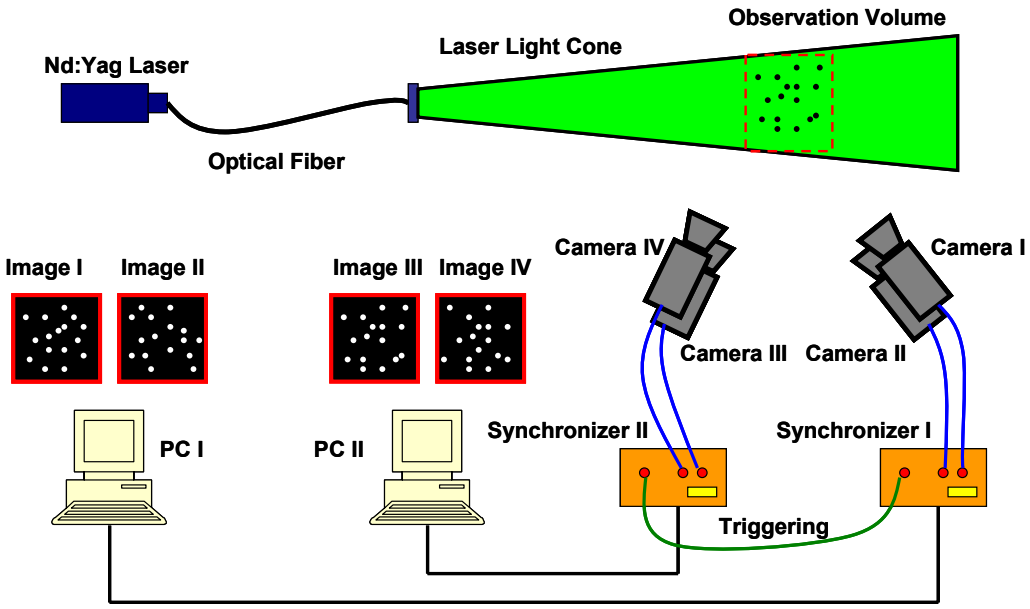

Figure 3.1. 3D-PTV data acquisition system

Figure 3.2. Photograph showing the rectangular arrangement of the four cameras. The four cameras were rotated and tilted to focus on the same region in the measurement tank (not shown)

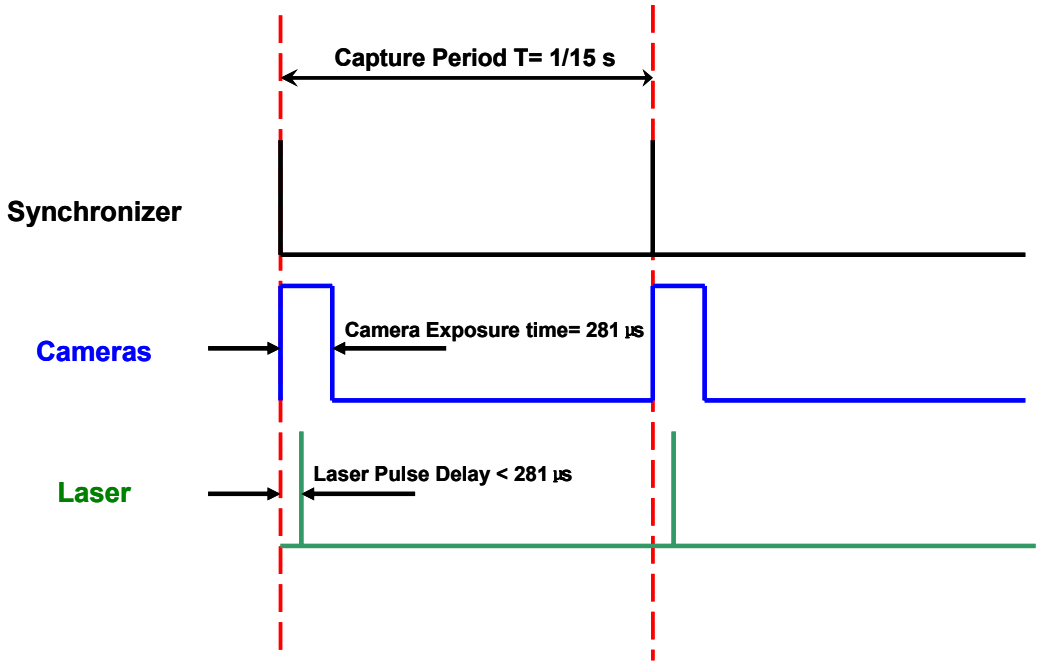

Figure 3.3. Imaging configuration between a synchronizer, two cameras and the dual pulsed laser

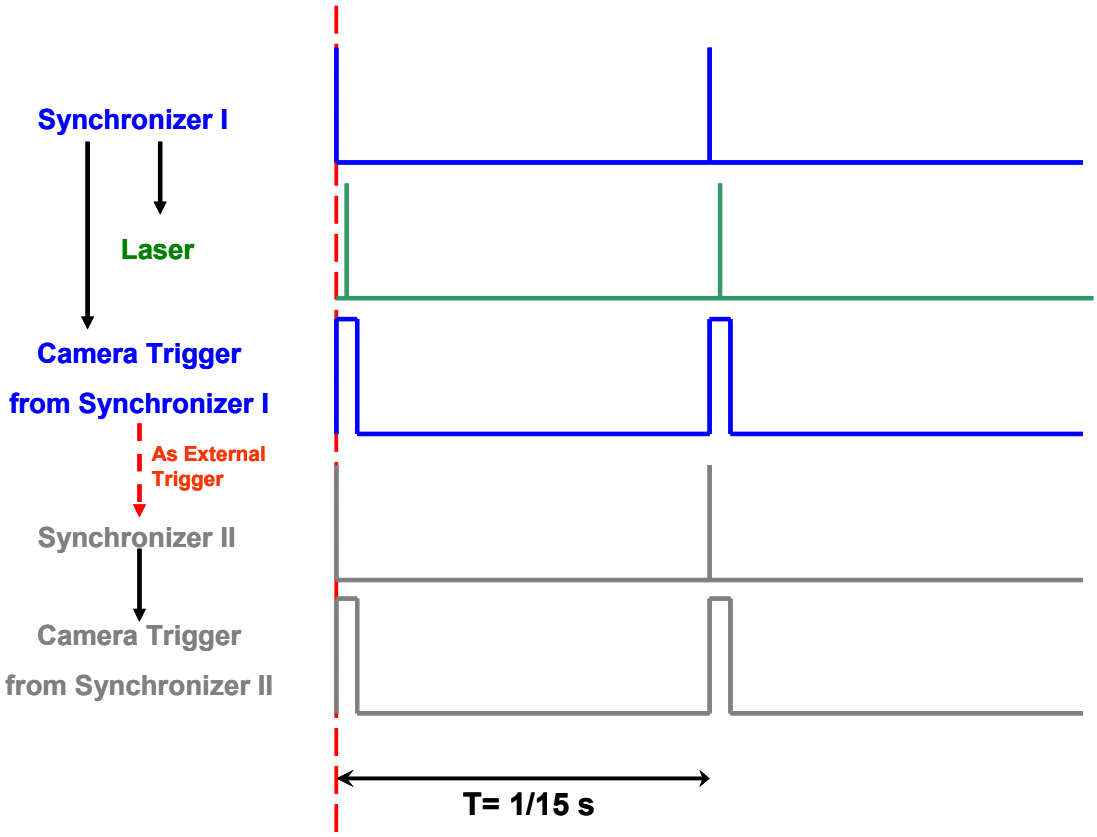

Figure 3.4. 3D-PTV system synchronization signals. In order to acquire four images simultaneously, two synchronizers were used. Synchronizer I initializes cameras I and II, the laser and synchronizer II. Synchronizer II initializes cameras III and IV.

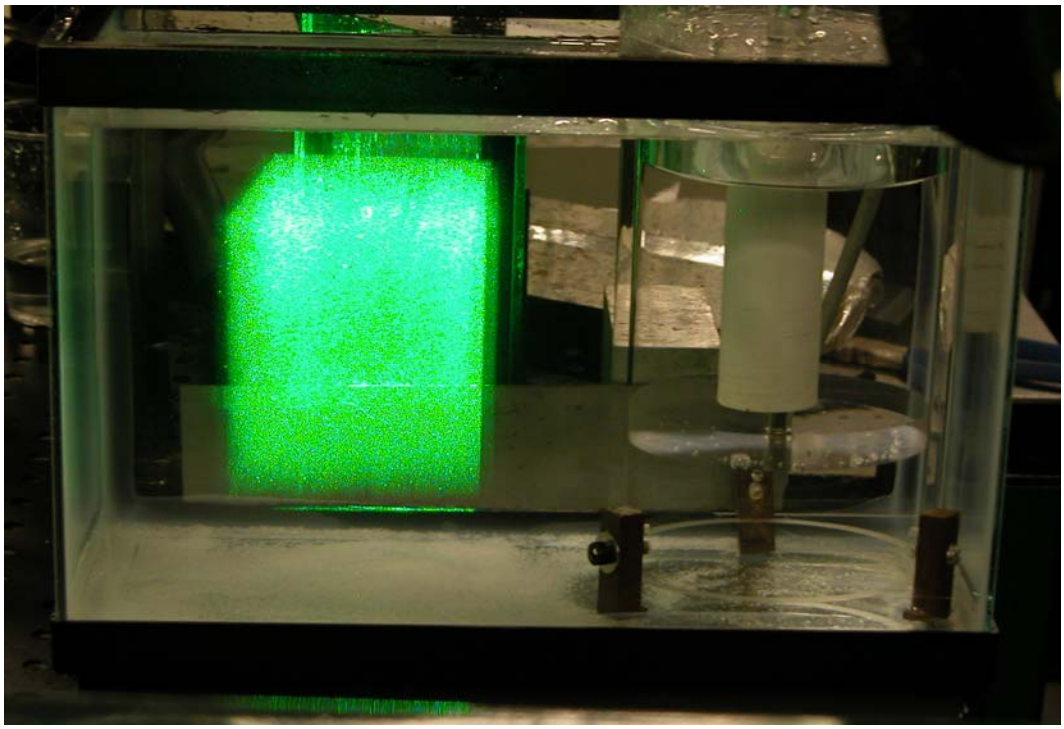

Figure 3.5. Photograph of the measurement tank showing the laser light illuminated volume

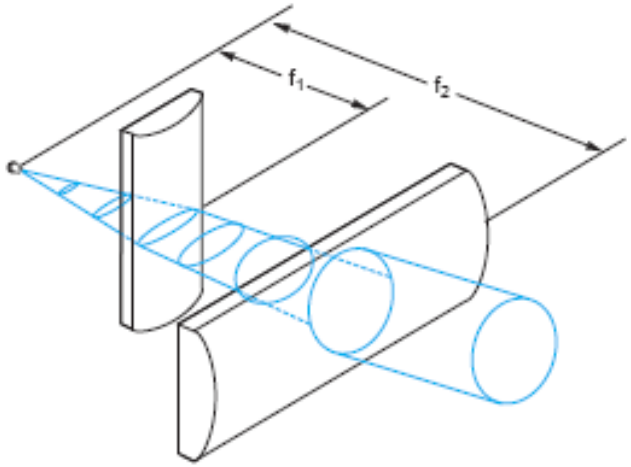

Figure 3.6 Laser beam expansion with cylindrical lenses

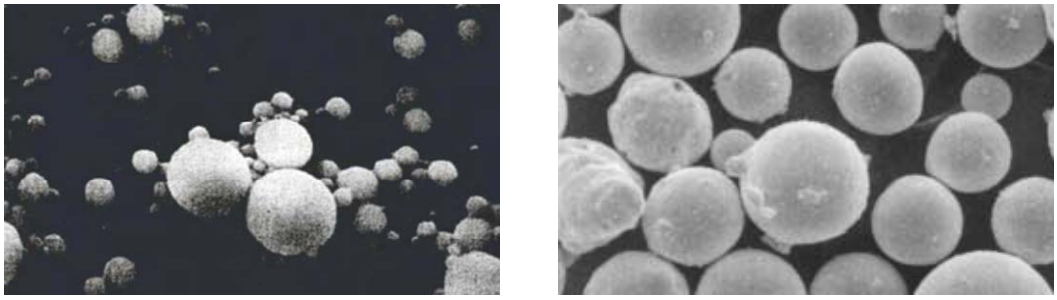

Aluminum Oxide Particles **Silver Coated Hollow Ceramics**

Figure 3.7. Microscopic view of tracer particles. [30]

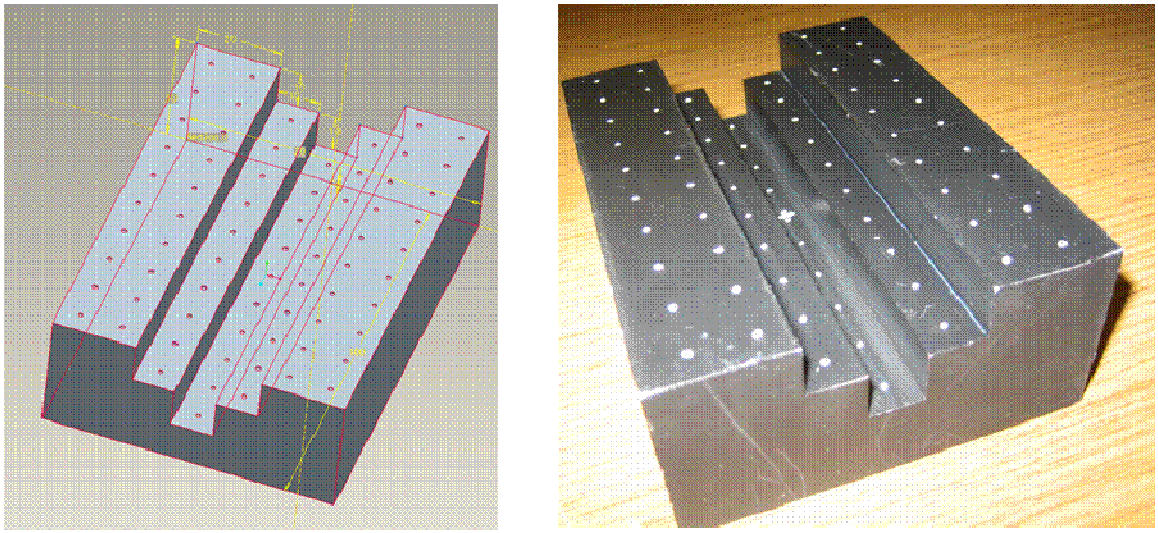

a) Calibration Target (CAD Drawing) **b) Calibration Target (Finished Product)**

Figure 3.8. Calibration target

Chapter 4

3D-Volumetric Viewing Calibration and Image Analysis

In this chapter, the 3D-Volumetric viewing calibration and image analysis for the 3D-PTV system are discussed. The experimental procedure is introduced first, followed by the explanation of the calibration procedure and image analysis.

4.1 Introduction to 3D-PTV Experimental Procedure

A flowchart of the main procedure for the 3D-PTV experiment is illustrated in Fig. 4.1. The first step in the experimental procedure is to determine the location and dimensions of the observation volume. The location and dimensions of the observation volume are determined based on the conditions of the flow field to be visualized and the 3D-PTV system itself, including, for example camera models, optical lenses, and laser light intensity. After the observation volume is determined, the four cameras are positioned and focused onto this volume. Further, two cylindrical lenses or a liquid light guide are positioned to expand the laser beam into a volume. The laser light volume is matched to the position and dimensions of the observation volume. Next the 3D-PTV system is

calibrated with the calibration targets detailed in Section 4.2. After calibration, several sets of sample images are taken to determine the capture rate, camera aperture, laser power, and particle seeding density based on the raw images and preliminary data processing. Lastly, adjustment is made on different particle identification and tracking parameters (e.g. estimated particle image threshold, particle size and particle displacement limit) and the final settings are used for the actual data set collection. These sets of experimental data are preprocessed in MATLAB and analyzed with the 3D-PTV software, while the results are processed and visualized in MATLAB and TECPLOT. Data analysis is explicated in Section 4.3.

4.2 4-Camera Viewing Calibration

The purpose of the calibration process of the 3D-PTV system is to obtain the coordinates' transformation information between the image coordinates and the world coordinates. The calibration is initiated by specifying the camera orientation, lens distortion, and laser light volume position and dimensions for the calibration software. Further, the calibration procedure is refined based on the initial estimate through geometric imaging (Ch.2).

4.2.1 Initial Calibration Estimation

The initial estimate of the camera orientation is done by the manual measurement of the translation and rotation angles of the camera axes based on the world coordinates. Fig.

4.2 illustrates the definition of world coordinates. The red coordinates (X, Y, Z) are defined as the world coordinate system, where the orientation O is located on the inner glass wall of the tank. As shown in Fig 4.2, the Z axis goes through the center fulcrum (white-cross) of the calibration target. The calibration procedures are as follows:

1) The calibration target is placed in the tank where the observation volume is. The center of the calibration target, marked by the fulcrum, is then placed close to the center of the observation volume. Further, an incandescent light source is used to illuminate the target.

2) The four cameras are set up to observe the same observation volume with the calibration fulcrum in the center of the four cameras area, and the image magnification in each camera as similar as possible. Further, the lowest f-number on the camera lenses is set to provide the largest lens aperture to maximize light collection. Each of the four cameras is then focused on the dots in the calibration target. As the calibration dots have different z-components, there is a possibility that not all of them can be clearly focused. When this occurs, the f-number of the lens was increased to increase the depth of field of the images at the expense of reducing the amount of light that reaches the CCD. Once the four cameras are focus on the entire target a set of images was taken. These are the images that will be use later on to generate the transformation matrix from world coordinates to camera coordinates.

3) The position and angle (X_c, Y_c, Z_c) of each camera lens' center was measured and recorded in world coordinates as shown in Fig. 4.2. Similarly, the position of the calibration target fulcrum was determined as (0, 0, Z_{crs}), where Z_{crs} is the distance from the fulcrum to the inner glass wall of the tank.

4) The calibration target is then removed from the tank. All other components of the setup such as cameras, lenses, and laser optics will remain fixed for the rest of the calibration process and actual experimental data collection.

4.2.2 Calibration Optimization

After taking the initial measurement of the camera orientations, laser volume location, and calibration dots locations, the values are modified by analyzing the target images based on geometric imaging principles. The procedure is detailed below:

1) The target images taken during the calibration process (Sec. 4.2.1 step 2) are filtered using custom programming in MATLAB. This is a mean filter that reduces the background noise for higher contrast between the white-dots in the target and its background.

2) Given the camera orientation and position from Sec. 4.2.1 step 3, the rotation matrix between camera body and world coordinates is calculated. A sample of the camera

orientation parameters for one of the four cameras is listed in Table 4.1. The camera projection center position is the distance from the camera projection center, which can be estimated as the center of camera lens, to the origin of world coordinates in mm. The camera body rotation angles are measured with a protractor and level tool in degrees. The rotation matrix as then computed from the three angles (θ_X, θ_Y, θ_Z).

Camera Orientation Parameters	Typical Values
Camera Projection Center C (X_c, Y_c, Z_c)	(-94mm, -44mm, 302mm)
Camera Body Rotation Angle (θ_X, θ_Y, θ_Z)	(12°, -14°,0°)
Calculated Rotation Matrix	0.971 0.000 -0.245 -0.049 0.980 -0.194 0.240 0.200 0.950
Image Axis Offset (x_p, y_p)	(-0.773mm, 1.02mm)
Camera Principle Distance	47.3 mm

Table 4.1. Typical camera orientation parameters in world coordinate and calculated rotation matrix

3) The principle distance is calculated using the following equation:

Principle Distance = (CCD chip dimension/Camera field of view dimension) x Z_c.

For the sample case given in Table 4.1, the CCD chip dimension was 9.1mm, the camera field of view dimension was 58mm, and Z_c was 302mm. This gives a principle distance of 47.3mm.

4) Custom software is then used to detect the location of the white-dots in the calibration images previously filtered in step 2. Typical location and order of the white-dots is shown in Fig. 4.3 for one camera calibration-target image. This process needs to be repeated for

the four camera calibration-target images. The white-dots need to be labeled in sequence and identified in each camera as shown in Fig 4.3.The labeling of the dots, shown in green in Fig. 4.3, starts in the lower left corner and increases from left-to-right and bottom-to-top. The red values illustrate the 3D positions of the calibration dots in world coordinates. The fulcrum determines the origin in X and Y. For comparison, the original, unfiltered image of the camera calibration-target used is shown in Fig. 3.8, where the distance between dots was 10mm.

5) As a final step, the 3D-PTV software from ETH provided a more refined camera position and orientation as well as labeling of the white-dots based on the information provided in the previous steps. As a note, to check the reliability of the calibration, the calibration images can be used as real particle images and the reference dots' positions can be reconstructed to be compared with the input.

4.3 Image Analysis

The image analysis procedure is demonstrated in Fig. 4.4. First, the sets of raw images are preconditioned with a MATLAB code written for image filtering and noise removal. The preconditioned images are then imported into the 3D-PTV software for possible particle detections in all four cameras. The detection is done by searching for connected pixels that meet intensity and number of pixels criteria set up for each camera. The next

step is the particle correspondence between four cameras, which identifies the image points of the same actual particle in different camera images. If the same particle can be detected in all four camera images, it is called a **quadruplet**. If the same particle is only detected in three of the four camera images, it is called a **triplet**. Both quadruplets and triplets are considered valid particles, since the ambiguity is sufficiently small with three camera configuration, as explained in Chapter 2. Particles only detected in two cameras are not considered valid particles and are discarded. The procedure for particle identification in the four cameras at one time step is followed by particle tracking at different time steps. When the same valid particles are identified at multiple time steps it is said that they are correlated in the time domain. This correlation is detailed in Section 4.3.2. Thus, the data analysis software provides the valid particles three-dimensional position at each time step. This information can then be used to calculate particle trajectories, 3D velocity field in a volume, velocity contour in planes, particle accelerations and vorticity.

4.3.1 Image Preconditioning

A raw PTV image is subjected to different types of noise and background intensity. The source of noise and background can be:

a) reflections from optical surfaces such as lens, mirrors, and glass walls etc;

b) light scattered from particles that are not in the laser volume or from the liquid itself; c) electronic noise of the CCD due to thermal effects or readout conversion noise [1]. A

typical raw particle image is shown in Fig. 4.5 (left). To eliminate the light reflected by the liquid itself or optical surfaces and the electronic noise from the CCD, a set of images of the illuminated volume without tracer particles was taken and average. This average image was then subtracted from the raw particle images. A local mean filter can be applied to 'sharpen' the images by subtracting the mean intensity of a small interrogation area (i.e.: 32x32pixels) from each pixel in this area [31]. The actual particle intensity in the images is not affected much by this filter (<5%) while the noise intensity is significantly reduced. The image after preconditioning is shown in Fig. 4.5 (right). This process increases the signal to noise ratio between the particles and the background.

4.3.2 Particle Tracking between Time Steps

After triplets and quadruplets are identified as valid particles, the particle correlation in time domain was applied. The flowchart procedure for this time domain correlation is illustrated in Fig. 4.6. Taken an instantaneous particle 3D position obtained from the valid particle identification process, the previous position in time and next position in time for this particle was estimated based on the approximate assumption of the velocity in three directions. Then the particle 3D position is back projected onto the image coordinates for each camera. If there is a matching particle on each camera at the both the previous and the next time step, the particle was considered to be valid in the time domain and its 3D position was recorded. The 3D position is again analyzed through the same procedure to acquire the information for the next time step. The 3D particle positions in adjacent time

steps are linked together and produce the trajectory of the particle.

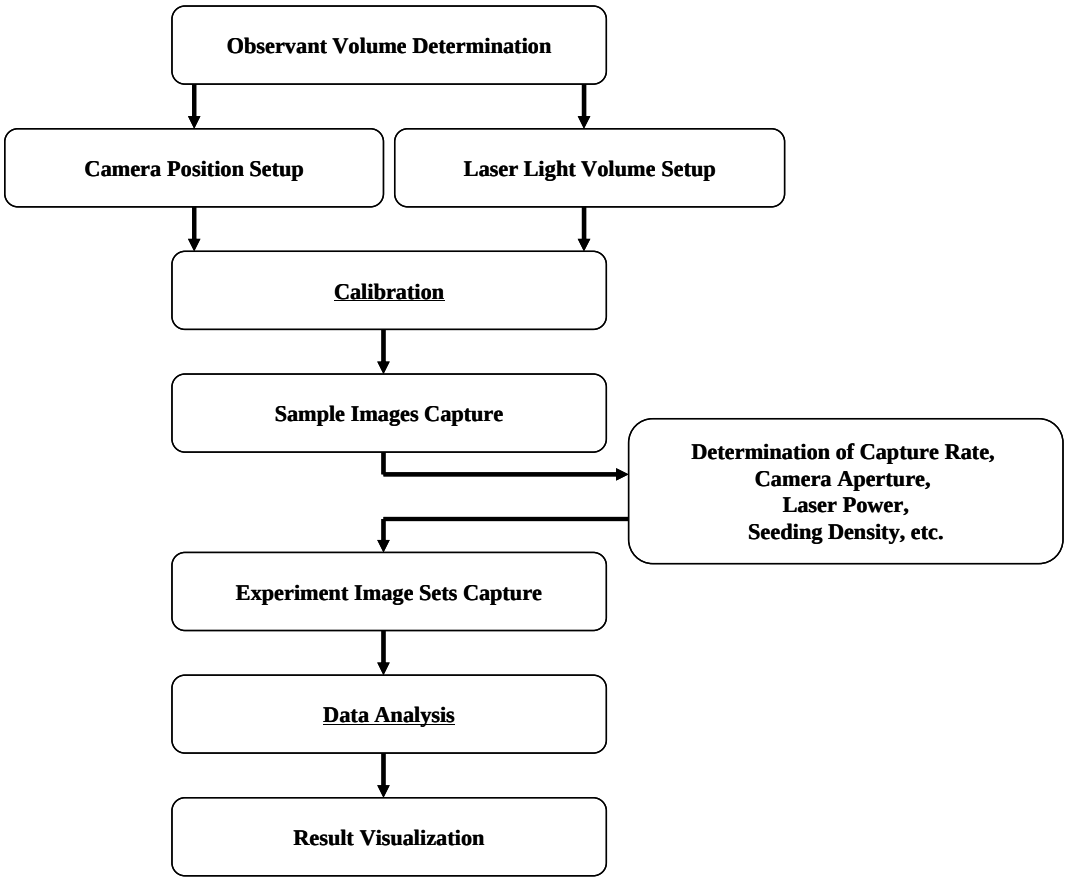

Figure 4.1. 3D-PTV experiment procedure

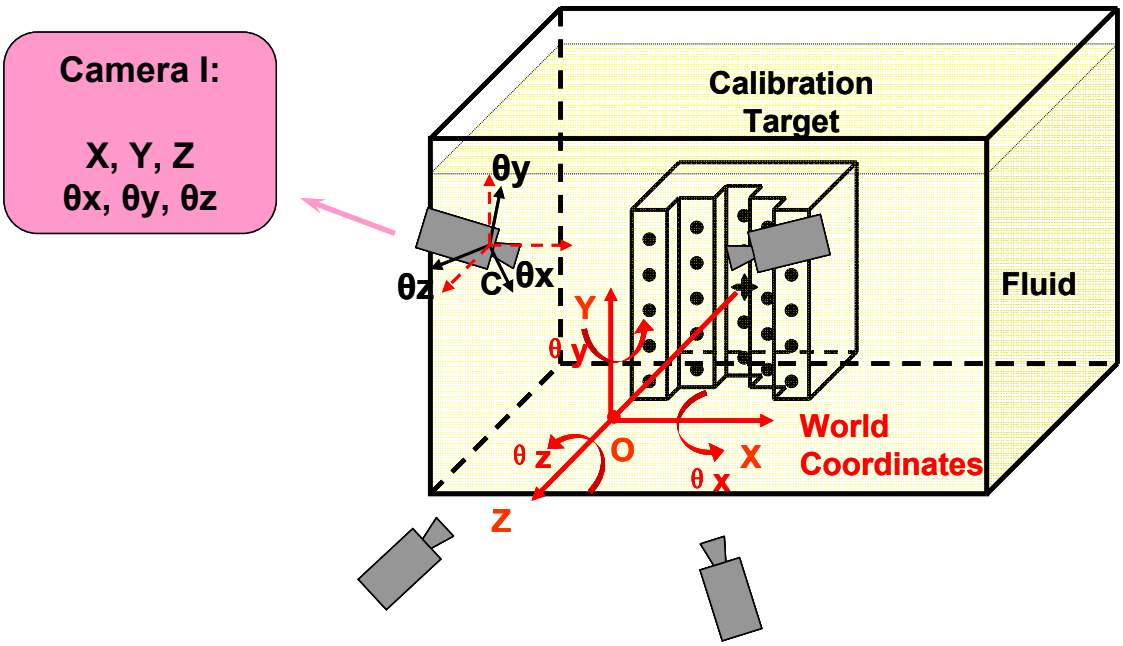

Figure 4.2. Definition of world coordinates.
The figure shows the location of the calibration target and four cameras in reference to the world coordinates.

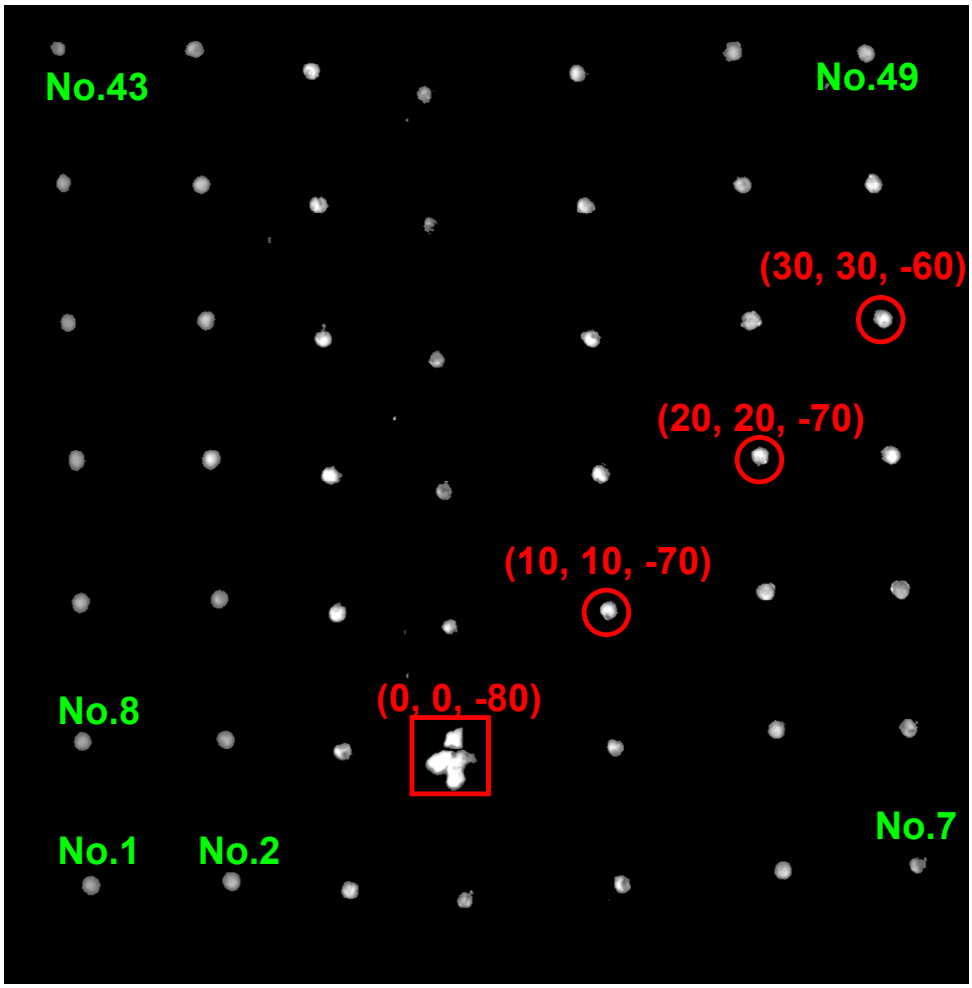

Figure 4.3. Sample calibration target image.
The white dots are labeled in ascending order starting in the lower left corner (green labels). The 3D position of the dos in world coordinates is shown for select dots in red. The fulcrum determines the origin in X and Y.

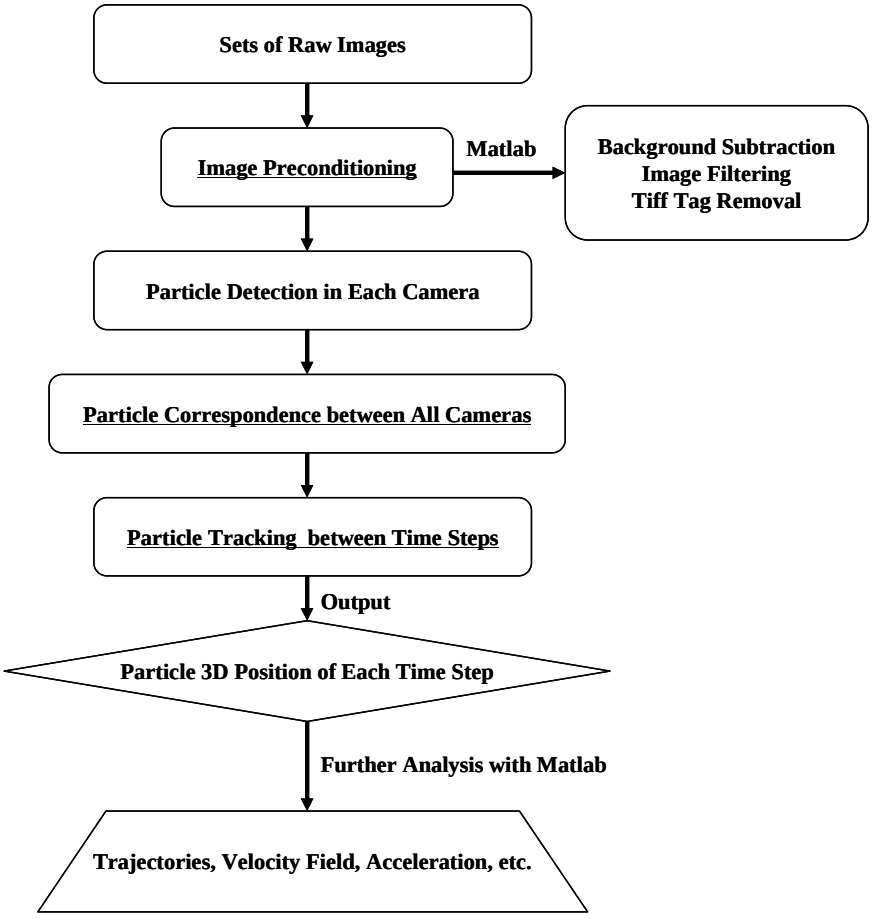

Figure 4.4. Image analysis procedure

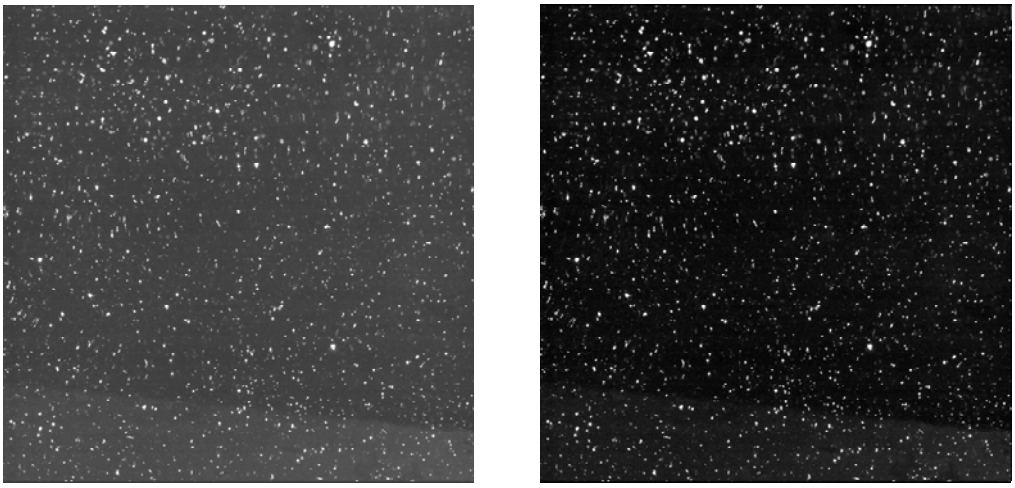

Raw Particle Image without Preconditioning

Particle Image after Highpass Filtering

Figure 4.5. Comparison of particle image before and after preconditioning

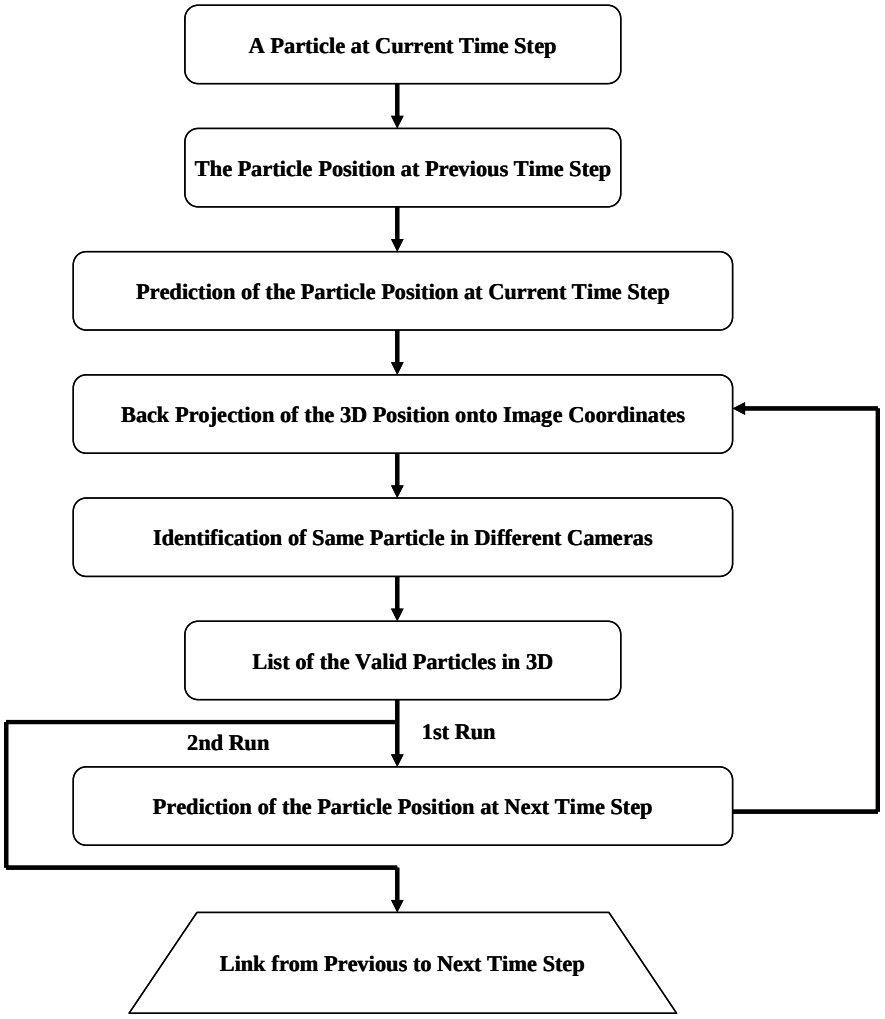

Figure 4.6. Tracking procedure (Correlations between time steps after correspondence)

Chapter 5

3D-PTV Accuracy

In this chapter, the tests of different hardware and software variables of 3D-PTV technique that affect the accuracy of the system are discussed. A piston system which generates a simple nearly one direction flow was used as the object to apply the tests. Both water and glycerin were used as the fluid media.

5.1 The Influence of the Calibration Target

The accuracy of the 3D-PTV system is largely limited by the results from the calibration procedure that will be described next. During this procedure, images of a calibration target are taken. The calibration target, as the reference body, is the most important factor of the calibration. As mentioned in Chapter 3, the target needs to have high contrast between the black background and reference white dots. Also the dots need to be preferably round and precisely located. Several calibration targets with different

dimensions and materials were tested, as listed in Table 5.1. The appearance of the targets is shown in Fig. 5.1.

	Target Description	Dimensions (mm)	Material and Properties	Advantages	Drawbacks
#1	TSI calibration target	200 x 200 x 1	Black anodized aluminum body; white dots with 1mm diameter	Commercial product; precisely located dots	Z-spacing between dots was too small
#2	Acrylic plastic target	100 x 100 x 10	Clear acrylic body; White markers on both sides	Increased z component dimension	Low contrast between acrylic and reference dots; the position of reference dots was not very accurate
#3	Prototype target I	70 x 100 x 30	Black painted prototyped body; Whiteout filled holes 2mm diameter	target proportional to measurement volume; ref. dots precisely located	Uneven dot shape; dot size too big; slight shadow around dots
#4	Prototype target II	70 x 100 x 30	Black painted prototyped body; Shinny paper pasted shallow holes 1.4mm diameter	target proportional to measurement volume; Evenly shaped dots	the position of reference dots was not very accurate ; not enough contract between dots and back paint
#5	Aluminum target	70 x 100 x 30	Black painted CNC machined	Good dimensions Evenly	--

			aluminum body; White paste filled shallow holes 1.2mm	shaped dots Well located dots	

Table 5.1. Evolution of calibration target

The quality of the target images is very important because the 3D-PTV software needs to recognize the location and size of the reference dots. Also, the dots need to be small enough and preferably round so that the software can detect the center of the dots correctly. Three of the targets tested, targets 2, 3, and 4, in Table 5.1, failed because of the low quality calibration images they generated. The TSI target gave good images, but it is designed for planar measurements and is not meant for volume calibration as the z component is very small. Target #5 provided the best images, with well defined dots that were easily recognized by the calibration software. Also, the depth of the target was comparable to the depth of the measured volume which provided the best resolution in the z-direction.

The test results regarding accuracy of the calibration targets are listed in Table 5.2. The aluminum target had the best accuracy especially on the z-direction.

Target	Calibration error based on reference positions
TSI Calibration Target	0.10% 0.16% 7.4%
Prototype Target I	0.21%

	0.16% 1.1%
Prototype Target II	0.25% 0.19% 1.34%
Aluminum Target	0.13% 0.16% 0.79%

Table 5.2. Accuracy of calibration targets

5.2 The Influence of the Observation Volume

The observation volume in 3D-PTV measurements is the volume that is illuminated by the laser light and is within the field of view of the cameras. The dimension of the observation volume depends on the specific experiment requirement and is also limited by the camera lenses, laser power, tracer particle size, and other 3D-PTV parameters. For instance, large observation volumes (i.e.: 20 x 20 x 20 cm^3) would require a high intensity laser for illumination and appropriate lenses with large depth of view. The size of the tracer particles would also need to be larger to remain a minimum particle image size that can be detected by the camera/software.

The camera field of view is determined by the camera CCD chip active area and the lens magnification. The CCD chip size is fixed for a specific camera, while the magnification is based on the distance from the lens to the object. For the Nikon 50mm f/1.8D lens used, the minimum focus distance is 0.45m, with a magnification of 1/6.64. The CCD chip size of the cameras used, Kodak Megaplus 1.0ES, is 9.1mm x 9.2 mm. Thus, the smallest

field of view of this camera/lens system is 60.4mm x 61.1mm.

The depth of field is another crucial parameter that influences the size of the observation volume and the quality of the results. When a lens is focused on an object, there is a zone behind and in front of the object that is rendered acceptably sharp. This zone is called depth of field. The extent of the acceptably sharp range depends mainly on the distance from the object to the lens, the aperture of the lens, and the definition of acceptably sharp when we are looking at the images. For 3D-PTV, the acceptably sharp appearance on the images should satisfy the particle minimum intensity and minimum number of pixels for valid particle detection. With a fixed camera configuration, to achieve larger depth of field, closing the aperture is the solution. However, when using higher f-number, the amount of light that reaches the CCD chip in the camera decreases. As the amount of light reaching the CCD decreases, higher laser power and better scattering properties of the tracer particles are required.

The 3D-PTV measurement system was tested with two different sizes of field of view, as shown in Table 5.3. The two experiments were taken using the same laser power. Therefore, for the larger field of view, the image quality is worse and it is harder to find particle correspondence between cameras. Better results can be obtained with larger field of view if bigger particles, higher laser power, larger depth calibration target or multi-plane calibration are used. In our experimental setup, an observation volume of 60mm x

60mm x 50mm gave the best results.

Observation Volume Dimension	3D Particle Correspondence Between Images Error	Quadruplets out of total valid particles	Valid links/Total Particles
130mm x 130mm x 70mm	0.25% 0.28% 0.92%	19.3%	45.4%
60mm x 60mm x 50mm	0.10% 0.11% 0.39%	29.2%	66.6%

Table 5.3. Test of observation volume size

5.3 The Influence of Particle Properties

As discussed in Chapter 3, the actual flow motion is observed using tracer particles. Therefore, these particles need to follow the flow and scatter enough light to be detected by the cameras. For the particle-detection software to be able to identify a particle in an image the particle intensity must be above the background noise. It is also preferred if the particle is round and with a minimum size of 2 x 2 pixels. For a fixed camera/lens magnification, larger particles would occupy more pixels in the image which is preferred as it is easier to correlate the same particle in different cameras. Bigger and brighter particles on the images come from good amount of light scattered by the particles. According to Mie Scattering Theory, the amount of light scattered by tracer particles is a function of the size of the particles, index of refraction ratio of the particle and the fluid, wavelength of the laser light, concentration of the particles in the fluid, and position

(distance and angle) of the camera with respect to the light been scattered by the particle.

Different types of tracer particles were tested in two different fluids: water and glycerin. Table 5.4 gives the list of particles that were tested in water. The test results indicate that the size of the particles needs to be in the order of 100 microns for large field of view, 60mm x 60mm x 50mm. The results also show that the silver coated particles have much higher intensity (i.e.: brightness) on the images compared to the non-coated ones.

	Density (g/cc)	Mean Diameter (microns)	Light Scattering Property	Test Results	Average Particle Image Size in pixels	Particle Intensity (8 bit camera, 255 max value)
Fluid						
Water	1.0		n=1.33			
Particles						
Hollow glass spheres	0.9-1.1	8-12	Good	Good passive flow tracer but particle pixel size was too small	2 x 2	50
Silver coated glass spheres	0.9	8-12	Better	Good flow tracer but particle pixel size was too small	2 x 2	60
Silver coated hollow ceramic spheres	0.9±0.3	100+-20	Better	Not a good passive flow tracer; Good particle pixel size	5 x 5	80

Table 5.4. Different tracer particles in water

Table 5.5 shows the test results of different particles in glycerin. The glass spheres have a better matching density, but the index of refraction is too close to that of glycerin. As a consequence, the particles do not scatter much light and appear to be 'invisible' in glycerin. The 3M microspheres have better matching density and good size too, but due to the roughness of the particle surface and the uneven shape of the particles, not enough light is scattered into the cameras. Aluminum oxide particles were the be best choice in terms of size and scattering property, but the high density difference between particles and fluid creates a slightly off vertical velocity. A quick test to study the sinking speed of the particles showed that it takes about 12 minutes for the 150 micron-size particles to cover the size of our interrogation volume (60mm in height) when they were placed in still glycerin. The error in our measurements due to the terminal velocity of the particles (due to gravity) is negligible when compared to the speed at which the actual experiment measurements were taken (15 Hz).

	Density (g/cc)	Mean Diameter (microns)	Index of refraction/ Light Scattering Property	Test Results	Particle Intensity (8 bit camera, 255 max value)	Average Particle Image Size in pixels
Fluid						
Glycerin	1.26		n=1.473			
Particles						
Glass spheres	2.48-2.52	300	n=1.51	Good passive flow tracer Similar index	50	--

				of refraction makes particle 'invisible'		
Aluminum Oxide	4.0	150	Good	OK passive flow tracer; Good particle pixel size	50	5 x 5 50
Aluminum Oxide	4.0	500	Good	Bad passive flow tracer; Good particle pixel size	60	7 x 7 60
3M Ceramic Microspheres	2.2	200	Bad	Do not scatter enough light	--	--

Table 5.5. Different tracer particles in glycerin

These tests with different particles clearly show the importance of properly matching the particle size, density, and index of refraction to the experiment at hand when doing PTV. A more detail analysis would be recommended to fully optimize the measurements. This would require access to a larger selection of particles for the study which was beyond the scope of this thesis.

5.4 The Influence of the Camera Configuration

Camera configuration is the arrangement of the multiple cameras in the 3D-PTV system in terms of their spatial location. The arrangement of the cameras has a great influence on the establishment of particle correspondence between images and the accuracy of the system. As discussed in Chapter 3, the reason for having three or four cameras for the 3D-PTV system is to decrease the number of ambiguities when identifying the same particle in different camera images. Studies of camera arrangement (Maas 1992) indicate

that for a three-camera system, the best arrangement is to have the three cameras positioned at the corners of an equilateral triangle, or in a collinearly in a line equidistant from each other [29]. For a four-camera system, the best arrangement is to have them in a square. During the actual experiments, the overlapped area between different camera images should be maximized and the image to object ratios of different cameras should be close from one another.

Different camera configurations were tested in this work. Some selected camera configurations are shown in Fig. 5.2, and the correspondent test results are listed in Table 5.6. To demonstrate the camera configurations, the camera orientation and rotation angles based on world coordinate system are shown in Fig. 5.3. The cameras were mounted onto two parallel horizontal bars, two on the top and two on the bottom. For the first case, the bottom two cameras were placed with small θ_y angles and close to each other, while the top two had larger θ_y angles with similar distance as of the bottom two. This configuration has the benefit of having larger overlapping field of view and larger number of correspondence. However, as the cameras are too close to each other, the calibration can not provide enough information about the z-component position, which increased the error of the z-component during the 3D particle position reconstruction. The second configuration shown in Fig. 5.2 separates the four cameras far apart so that the volume can be observed from very different perspectives. Since the top two cameras are farther apart from each other, it made the size of their observed field of view bigger than

the bottom two cameras. To reduce this, they were moved forward to decrease the difference between the sizes of their field of view. This configuration provided the highest accuracy when determining the X, Y, Z position of the particles, but the number of particle correspondence decreases due to the distortion and particle light scattering properties observed from different camera orientation/position. The third configuration has the four cameras in a square arrangement with similar θ_x and θ_y angles. This configuration was a compromise between trying to provide a larger overlapping field of view between the four cameras and also trying to provide different camera perspectives. This setup provided a better results regarding particle identification between camera images and accuracy of z component reconstruction.

Camera Configuration	3D Correspondence Error	Quadruplets out of total valid particles	Valid links/Total Particles
First Case	0.27% 0.34% 1.31%	49.8%	26.2%
Second Case	0.10% 0.13% 0.53%	6.56%	54.8%
Third Case	0.10% 0.11% 0.39%	29.2%	66.6%

Table 5.6. Test results for different camera configuration

The camera arrangement in reference to the laser light direction is another important factor in 3D-PTV measurements. Due to the Mie Theory of particle light scattering, the amount of light scattered by the particles that reaches the camera is related to the camera

position and to the light direction. Backscattering provides much more light than forward scattering does. Hence, the ideal case is to have the cameras facing the coming laser light with small angles, as shown in Fig. 5.4. For the 3D-PTV system, this configuration creates a major problem. That is, the whole z component inside of the tank will be illuminated. This makes the identification of particles very hard, because even if the camera f-numbers are large to have less depth of view, the depth of view is still hard to define. This means all the particles in the tank along the z-direction will be seen on the images in either clear or blurred state, and thus the particles are hard to be separated from such high background noise. Also, the size of the observation volume is unclearly identified. A possible solution for this is to have a very thin tank, and then the whole width will be the depth of the observation volume. Another solution is to have some transparent media with the same index of refraction as the liquid to separate the observation volume, and particles are only seeded in the boxed areas. Both solutions will limit the application of the 3D-PTV system. The final camera arrangement used in this work consisted of the four cameras on the same side of the laser beam. The intensity difference between backscattering and forward scattering was solved by using different aperture and during image preprocessing.

5.5 Description of the Test Object for 3D-PTV System

All the tests of the different configurations shown in sections 5.2-5.4 were done on a 1-D

flow. The flow was created by a piston system as shown in Fig. 5.5. The piston was constructed in acrylic and had an inside diameter of 11cm. The piston was actuated manually in the vertical direction. The piston system was placed in a 30cm x 15cm x 18cm tank filled with glycerin. When the piston moves up, glycerin was drawn into the cylinder through the bottom of the cylinder (notice that the cylinder was elevated from the bottom of the tank by using 4 small metal blocks). This piston motion raised the level of glycerin inside the cylinder chamber and lowered it outside. The observation volume was located outside the piston system in the center of the small tank as shown in Fig. 5.5. The final observation volume was 60mm x 60mm x 50mm.

The actual velocity of the fluid outside the cylinder was calculated formulas follows:

$$v = v_0 \times \frac{\pi r^2}{lw - \pi r^2}, \tag{5.1}$$

where r is the radius of the piston, l is the length of the tank, w is the width of the tank, and v_0 is the velocity of the piston.

5.6 Test Results

The 3D-PTV system was tested with the quasi 1-D flow discussed above. A comparison of the data statistics with the sample work from ETH is listed in Table 5.7. The much larger observation volume used in the current work, made particle identification and correspondence much harder, but test results still show good agreement with the work at

ETH. If better tracer particles and higher laser power was available, the test results could potentially be improved. Further results of our system regarding the generation of 3D velocity field will be discussed in Chapter 6.

	Our 3D-PTV System	ETH Sample
Percentage of quadruplets/valid particles	26%	48%
Links/particles	68%	65%
Correspondence Error	0.10% 0.11% 0.39%	0.05% 0.05% 0.16%
Dimension of Observation Volume	60mm x 60mm x 50mm	20mm x 20mm x 20mm

Table 5.7. Test results comparison with sample work from ETH

Visualization of typical trajectories of the particles in 3D and 2D for the piston setup are shown in Fig. 5.6 & 5.7. Results showed that the displacement of particles between two time steps was the same as the calculated theoretical value for the piston system.

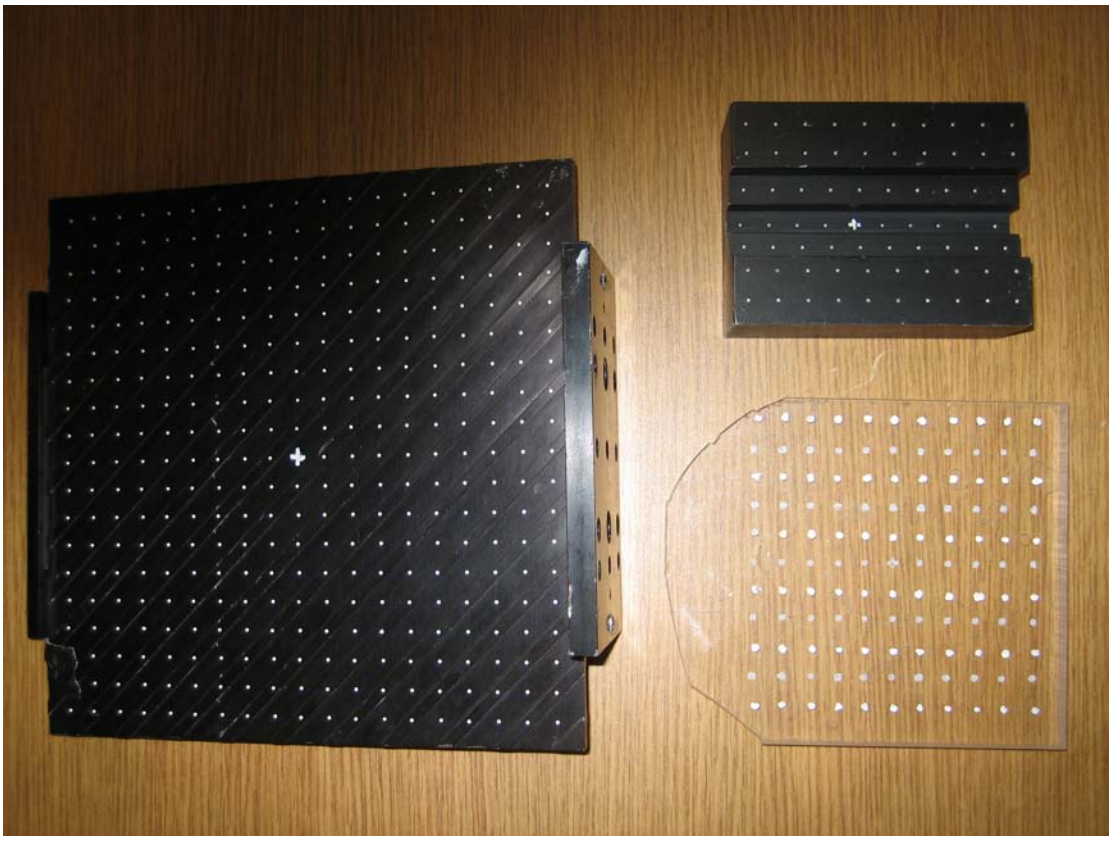

Figure 5.1. 3D calibration targets used to study the effect of different target types on the accuracy of 3D-PTV measurements.
The full list of targets is shown in Table 5.1. The one shown on the left corresponds to Target #1 on Table 5.1. the one on the lower right correspond to Target #2, and the one of the top corresponds to Target #5

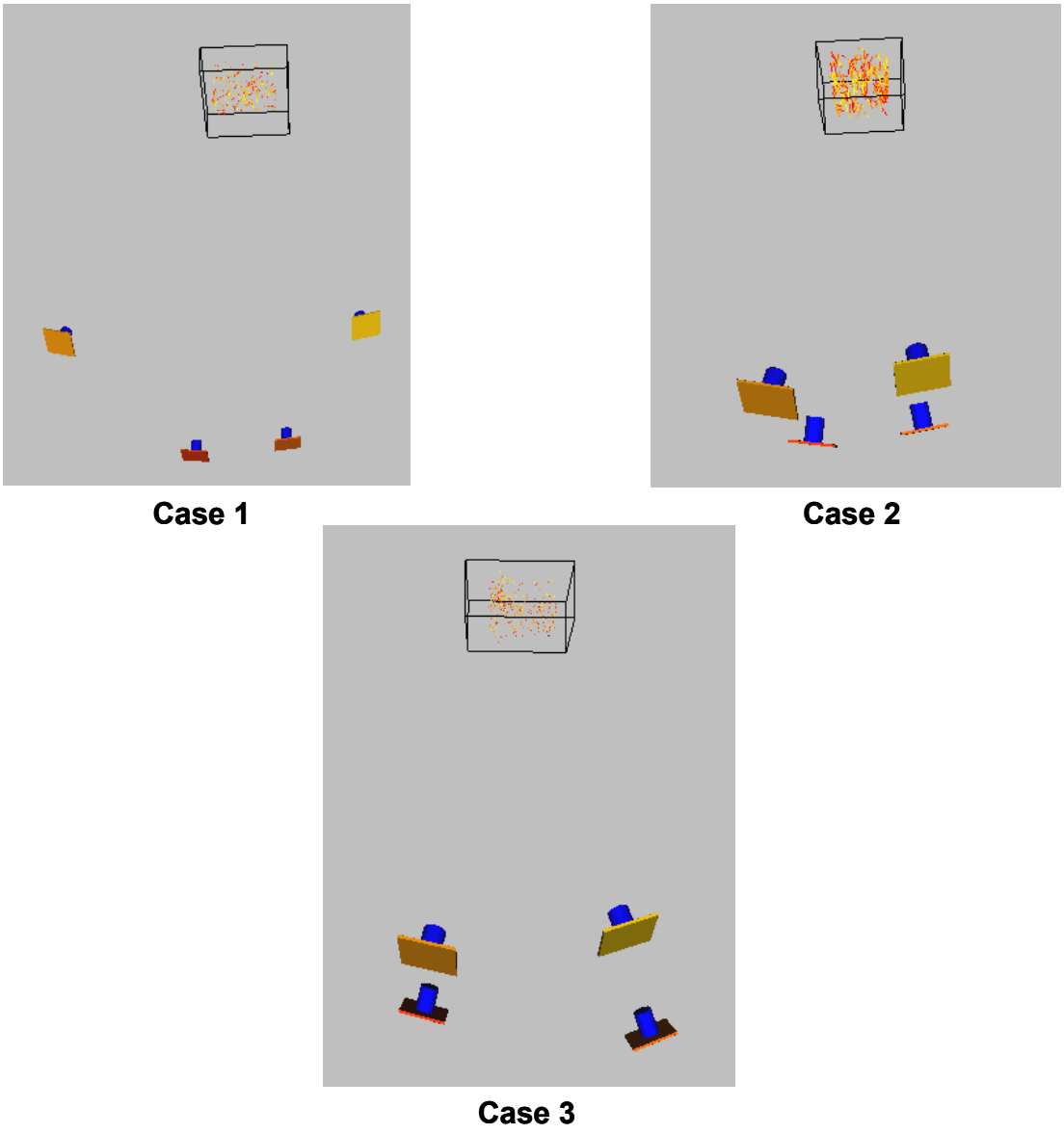

Figure 5.2. Three different camera configurations tested to study their effect on the accuracy of the 3D-PTV measurements

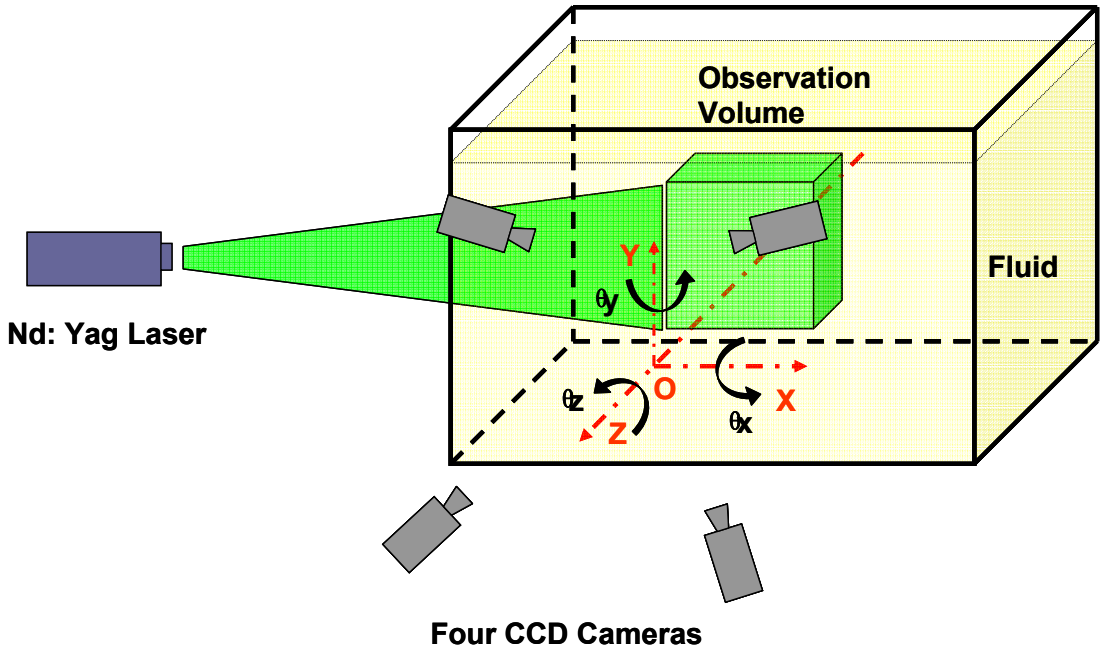

Figure 5.3. World coordinates for the 3D-PTV system

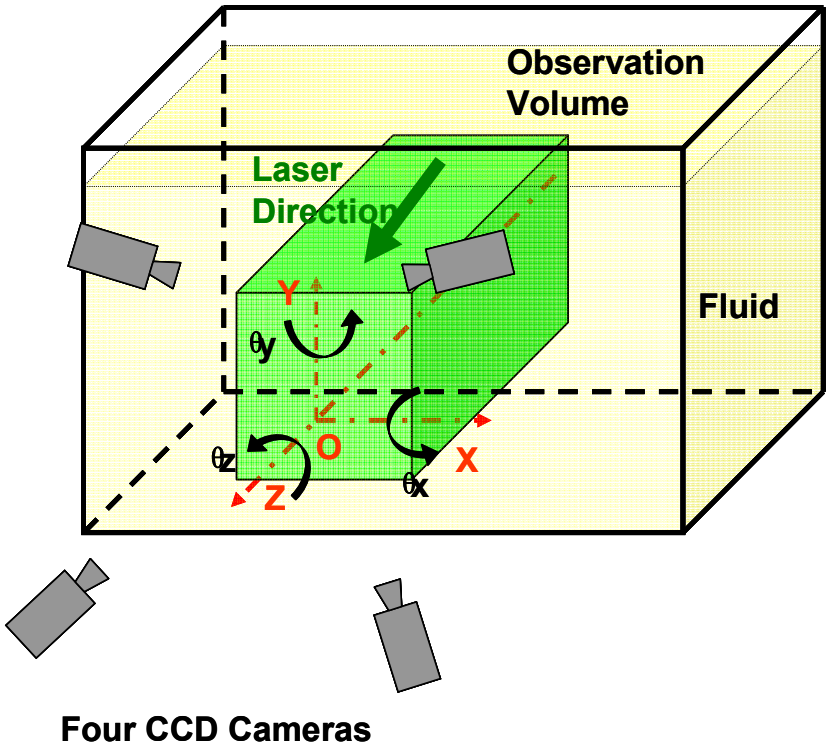

Figure 5.4. Cameras recording light scatter by particles in what is known as forward scattering mode

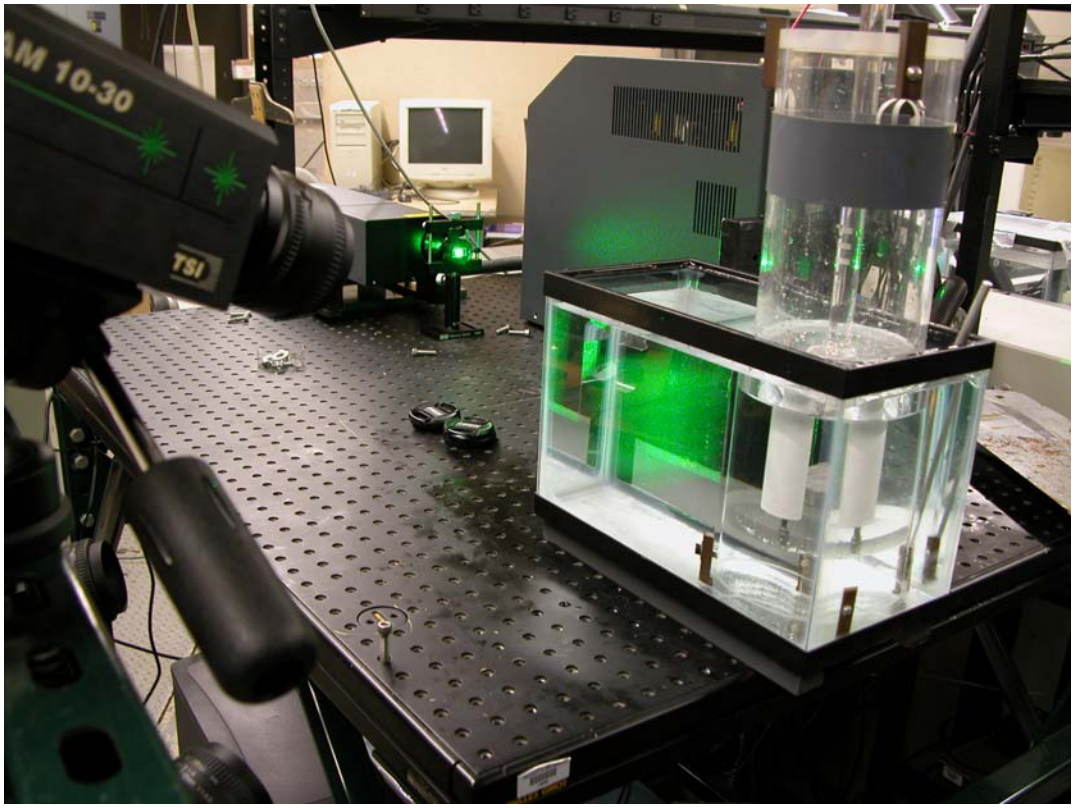

Figure 5.5. Photograph of the experimental setup showing the measurement rectangular tank filled with glycerin, the acrylic piston and the laser light illuminated interrogation volume

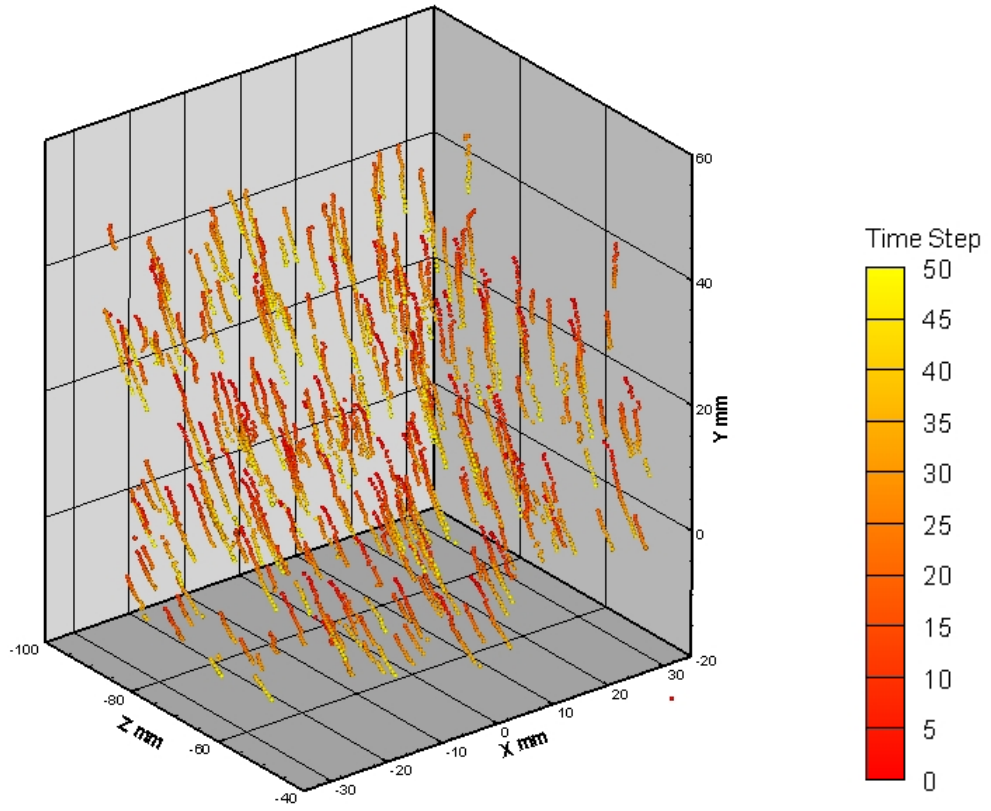

Figure 5.6. 3D view of 3D particle trajectories in a volume for different time steps. Different time steps were represented with different colors. All the particles are moving with an upwardly vertical trajectory. Flow was generated by a vertically moving piston.

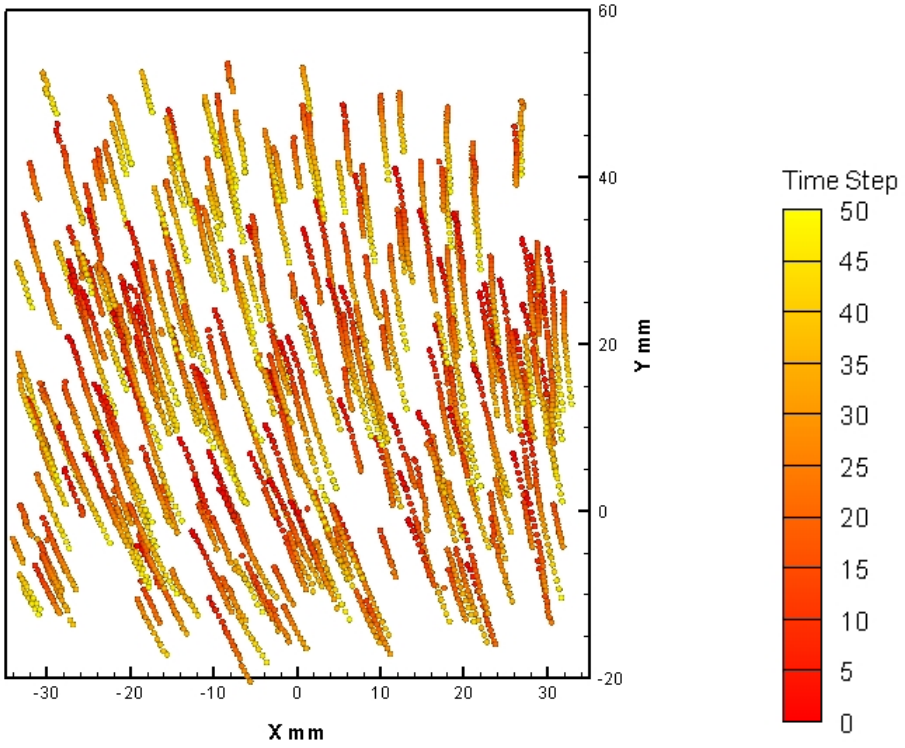

Figure 5.7. 2D view in the XY plane of 3D particle trajectories in a volume for different time steps Flow was generated by a vertically moving piston

Chapter 6

3D-PTV measurements compared with 2D PIV Measurements

In this chapter, the 3D-PTV measurements are compared and validated with measurements from a conventional 2D-PIV system. The measurements were done on a rotating flow inside a rectangular chamber. The velocity field in the 3D-PTV system is obtained from individual particle positions at different time steps, while the velocity field of in the 2D-PIV system is gained directly from correlation algorithms. This chapter includes the description of the experimental conditions, velocity field results from 2D-PIV, and comparison with the velocity field results from the 3D-PTV system.

6.1 Experimental Setup

6.1.1 Stirred Tank Setup

The setup consisted of a rectangular tank with an opening on the top and filled with glycerin that was stirred by using a rotating rectangular paddle. Fig. 6.1 shows the actual

experimental setup. The stirrer is made of acrylic with dimensions of 51mm x 51mm x 23mm. Fig. 6.1 shows the position of the stirrer which is driven by a gear motor. The rotation speed of the motor was proportional to the voltage input which allowed for an easy calibration and variation of experimental conditions. For the PIV and 3D-PTV comparison test, the input voltage was 9.7V which corresponded to a stirrer constant speed of 0.1rad/s. Aluminum oxide particles of 150micron diameters were used as the tracer particles in the tank for both PIV and PTV experiments.

6.1.2 2D-PIV System Setup

Fig. 6.1 shows the experimental setup for the 2D-PIV system. It consisted of an Nd: YAG laser (New Wave Solo PIV), one CCD camera (Kodak MegaPlus ES 1.0), a synchronizer (TSI 610034 LASERPULSE Synchronizer), and a PC loaded with TSI Insight 3G software. The capture rate of the system was 15 image pairs per second. A cylindrical lens and a spherical lens were used to create a thin laser sheet to illuminate the imaging plane shown in Fig. 6.2a. This is in contrast to the observation volume that was used for the 3D PTV measurements and shown in Fig. 6.2b.

6.1.3 Observation Area for PIV and Volume for PTV Experiments

Fig. 6.3 shows the location of the observation volume for the 3D-PTV measurements in reference to the stirrer. The observation volume had dimensions of 60mm x 60mm x 50mm Fig. 6.3 also shows the two observation planes where the 2D-PIV measurements

were made. The two horizontal planes (XZ plane) were located across the side of the stirrer, and the imaging area had dimensions of 60mm x 60mm.

6.2 Flow Field Results for 2D-PIV Measurements

For the PIV measurements, 20 Sets of 50 images pairs were taken. Fig. 6.4a shows a typical instantaneous velocity magnitude contour plot obtained with the PIV system. Fig. 6.4b shows the average velocity magnitude (50 images) contour plot. These figures show, first of all, that the flow is laminar and is moving in the clockwise direction with the stirrer. Also, the highest velocity occurs near the center, X = 0, where the axis of the stirrer is, and it decreases radially outwards. As expected, the velocity magnitude is symmetric around the stirrer's axis. The largest velocity magnitude was measured near the edge of the stirrer at about 16mm/s (shown in red in Fig. 6.4a&b). As expected, this is very close to the speed of the outer edge of the stirrer, which was calculated at about 16.9mm/s (0.1rad/s x 2π x 27mm). This shows that the fluid that is adjacent to the stirrer moves closely with the stirrer. As indicated, the velocity decreases radially outwards with the fluid flow and it barely moves just about 50mm away from the edge of the stirrer. A similar experiment was done by substituting the working fluid (glycerin) with water. It was interesting to note that the water barely moved even near the stirrer when this was moving at a maximum speed of 16mm/s. This is due to the difference in viscosity of these two fluids. The high viscosity of glycerin (~800 greater than water at 30°C) bears higher

friction and helps the motion of the stirrer to spread farther.

PIV measurements were done at two different planes parallel to each other as shown in Fig. 6.3. Mean velocities were then calculated by averaging 50 instantaneous velocity fields at each plane. Fig. 6.6a&b compared the mean velocity fields at the two planes. Both velocity fields are almost identical, which indicates that the flow is 2D in the vertical direction within the height of the stirrer. Measured mean velocity profiles along the x-direction at several z locations are also shown in Fig. 6.6a. Also, the measured mean w-velocity and u-velocity profiles along the x-direction at several z locations are shown in Fig. 6.6b and Fig. 6.6c respectively.

It was also observed that the velocity magnitude also decreases with larger z locations (farther from the stirrer). Fig. 6.6a&b show similar trends with the velocity decreasing at larger z-locations. It can also be noticed that the u component velocity is always larger than zero since the stirrer rotates clockwise dragging the fluid in that direction.

6.3 Comparison of 2D-PIV and 3D-PTV Measurements

Next the velocity field obtained from the PIV measurements is compared with the trajectories from the 3D-PTV system. Fig. 6.7 shows the individual particle trajectories for 50 time steps from 3D-PTV. The different colors (red to yellow scale as time increases)

represent different time steps, indicating the particle trajectory. Particles are rotating clockwise in the direction of the stirrer, describing a circular trajectory. Qualitatively, these trajectories show a good agreement when compared with the velocity profiles shown in Fig. 6.4b, which were attained from the 2D-PIV system.

A closer validation can be made by comparing the velocities obtained from the two methods. Fig. 6.8 shows the velocity comparison between 2D-PIV and 3D-PTV for the same flow conditions and at the same locations. The solid lines represent the PIV-obtained velocity values along the x-axis. The 3D-PTV obtained velocity values along the x-axis are shown with the symbol "*". The 3D-PTV velocity measurements were obtained from the 3D position of individual particles that were tracked at different time steps. The number of particles tracked at any given time was between 200-400 particles. Therefore, at any given z-location only a few particles were found using 3D-PTV, as shown by the "*" in Fig. 6.8. This figure compares the velocity magnitude, u-velocity and v-velocity for the two experimental methods. In general both methods showed a good agreement. Thus, the results indicate that the 3D-PTV and PIV techniques observed the same flow motion, with similar magnitudes and flow behavior. Finally, it was observed that the trajectories described by the particles shown in Fig. 6.7 are not entirely circular as would be expected from the PIV measurements in Fig. 6.4. This figure shows circular rings at different radial distances from the stirrer. It is expeculated that the seeding particles might increase and decrease their speed depending on the position of the stirrer.

This periodic motion can not be captured by the PIV system which averages the variation of the velocity at each position for different time steps.

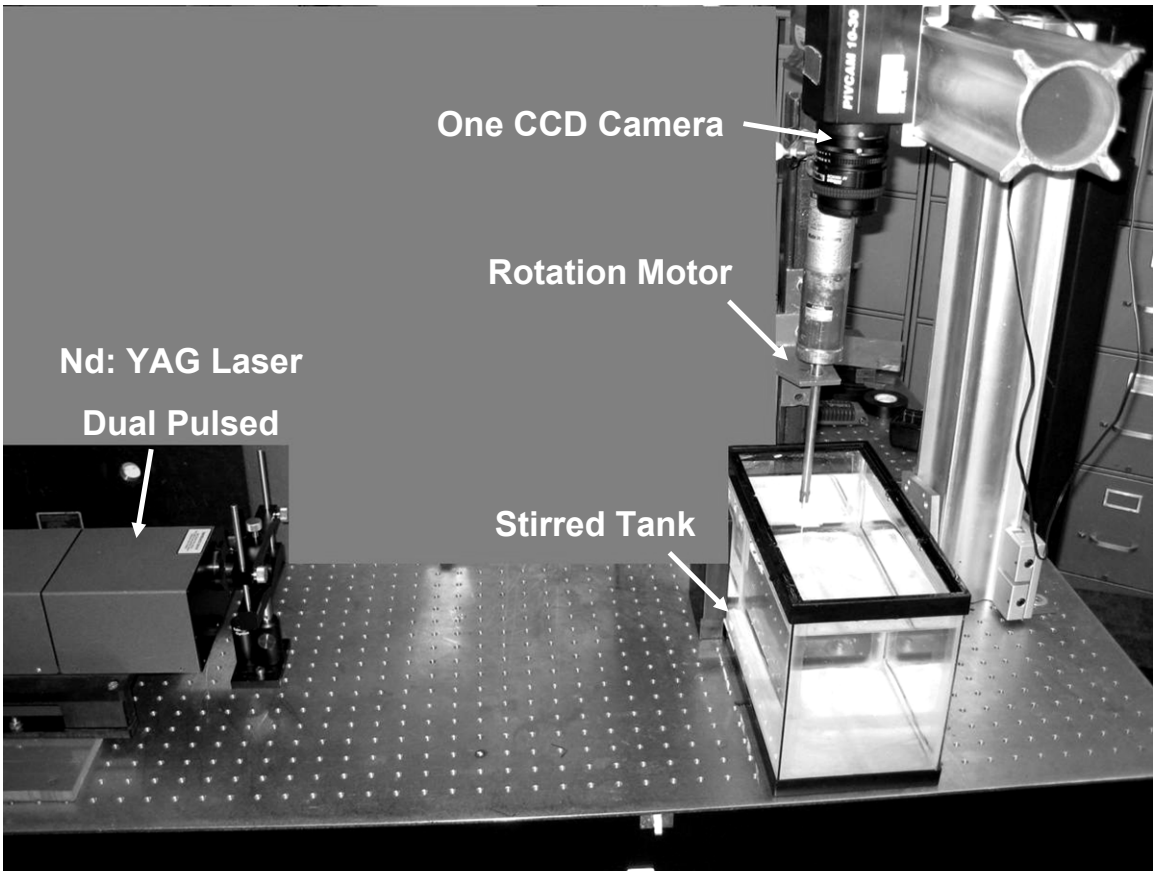

Figure 6.1. Experimental setup of 2D-PIV system
Laser sheet is horizontal across the side of the stirrer, the stirrer is connected to a gear motor, and the camera is mounted vertically to capture the top view of the flow around the stirrer.

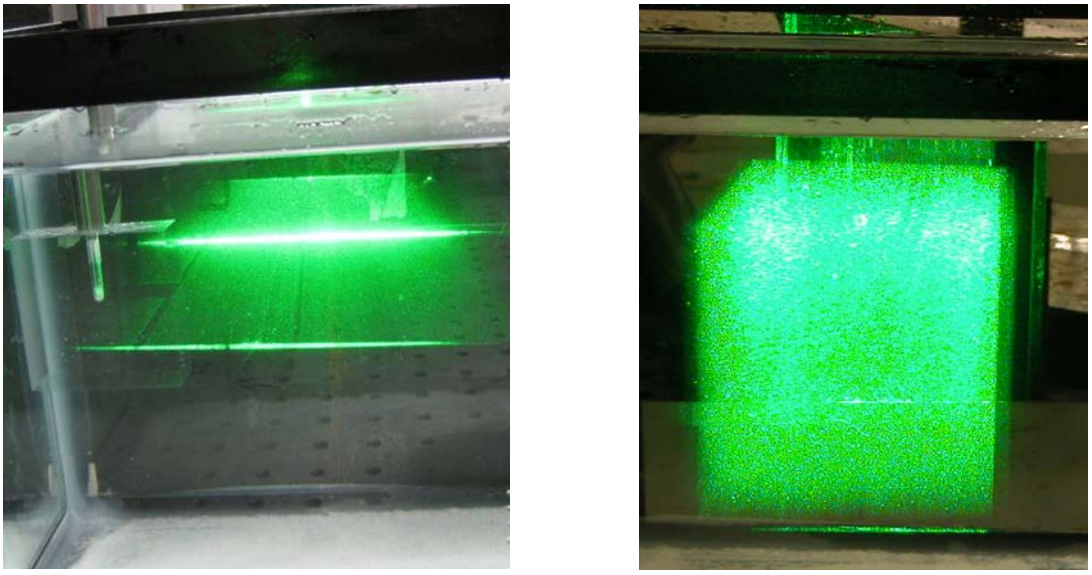

2D-PIV Illumination Plane **3D-PTV Illumination Volume**

Figure 6.2. Comparison of laser illumination of 2D-PIV and 3D-PTV
Left--Thin laser sheet for 2D-PIV. Only capture flow movement in a 2D plane.
Right--Laser volume for 3D-PTV. Capture flow movement in a 3D volume.

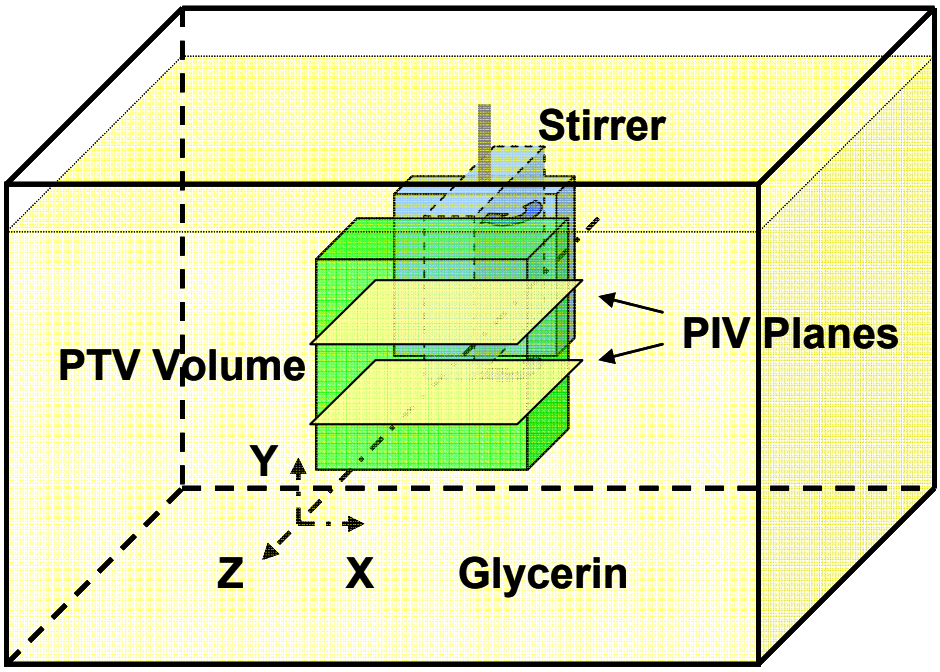

Figure 6.3. Location of the observation planes and volume
The stirrer is rotating clockwise behind the observation volume used in the 3D-PTV measurements (green cube). PIV measurements were performed at two horizontal planes.

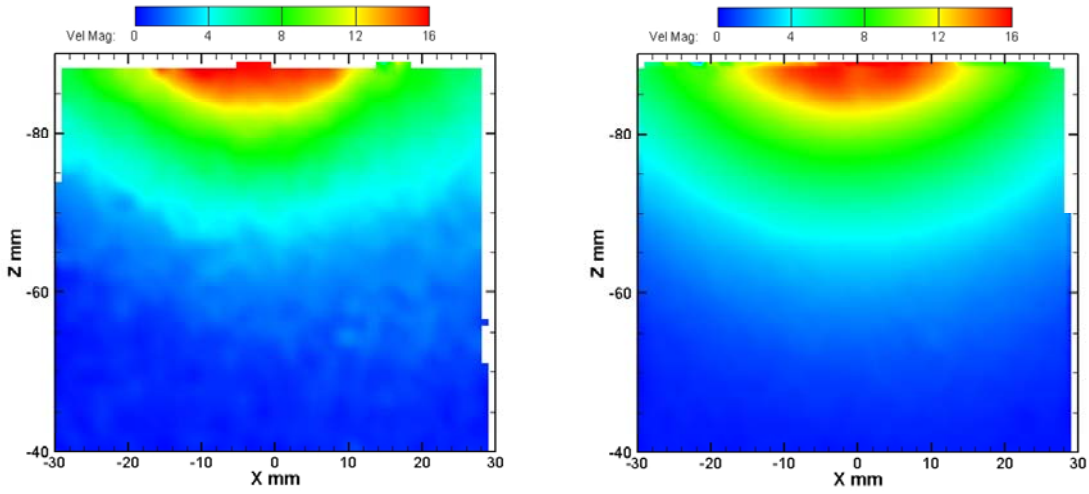

a) Instantaneous Velocity Magnitude **b) Mean Velocity Magnitude**

Figure 6.4. Velocity magnitude contour plot from PIV measurements
a) An instantaneous velocity contour plot
b) Mean velocity field of 50 images

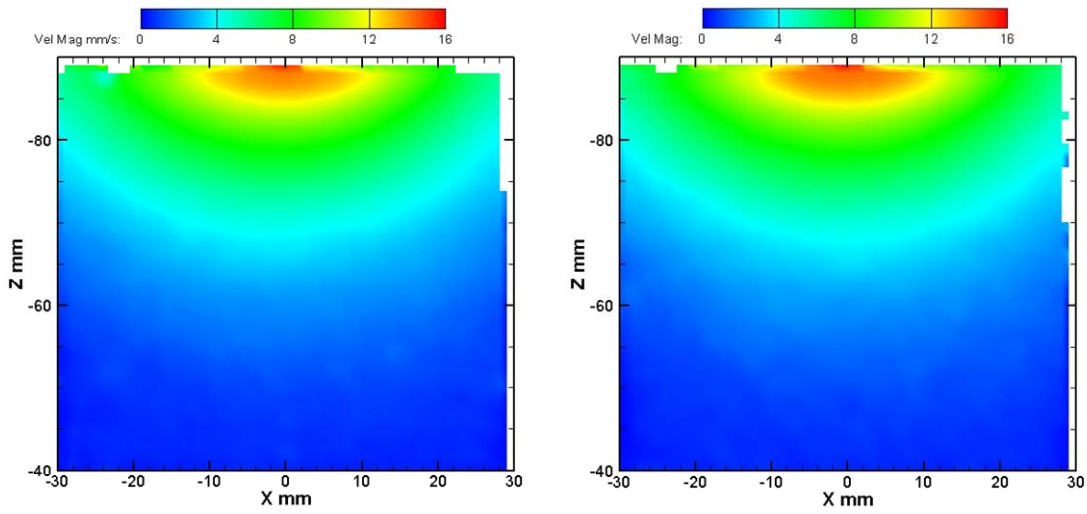

a) Top Plane **b) Bottom Plane**

Figure 6.5. Velocity magnitude contour plot at two planes
a) Top plane; b) Bottom plane.
They are almost identical as they are under identical conditions and the flow is two dimensional in the vertical direction.

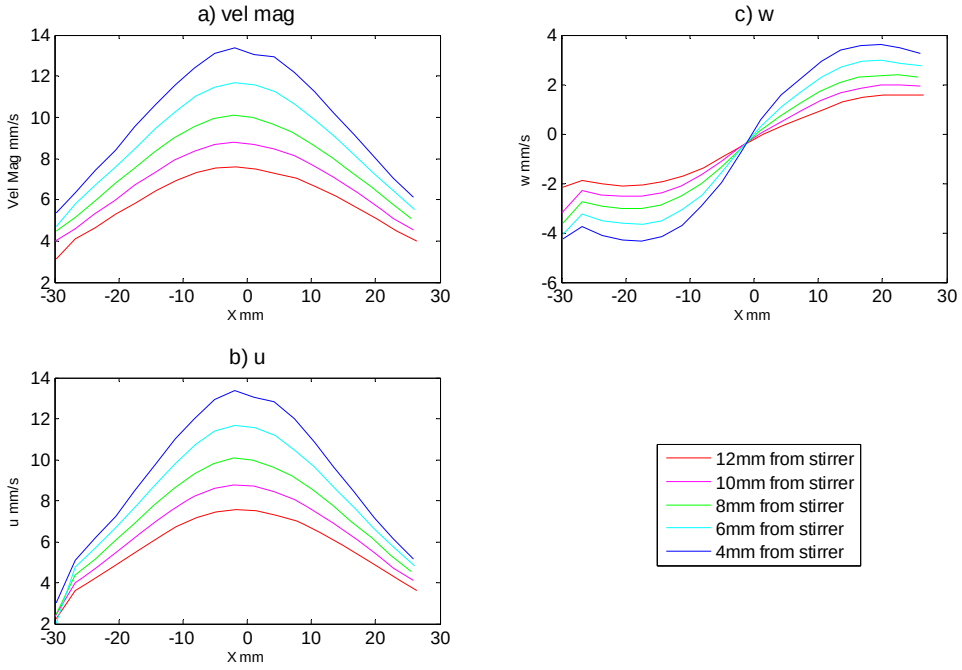

Figure 6.6. Velocity plots vs. locations along x direction
a) Velocity magnitude; b) X direction velocity u; c) Z direction velocity w
The different lines in the same plot are taken from different z locations

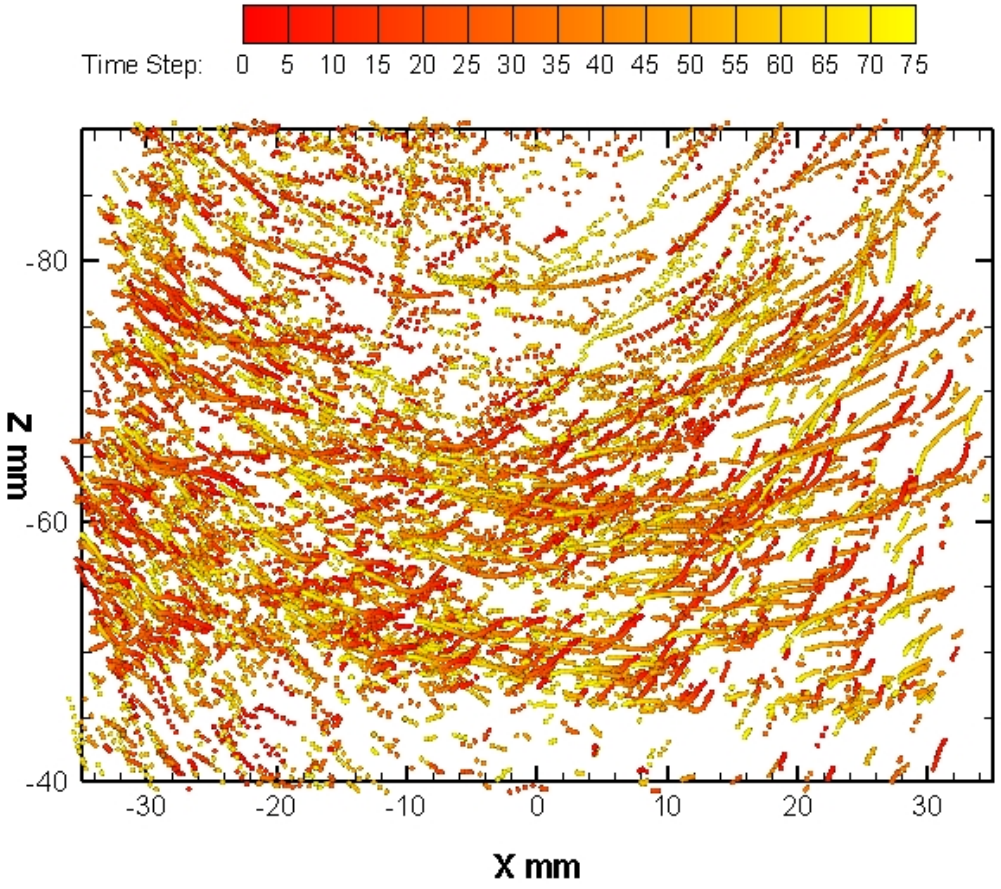

Figure 6.7. Top view (XZ plane) of 3D-PTV particle trajectories
Trajectories start from red and go to yellow

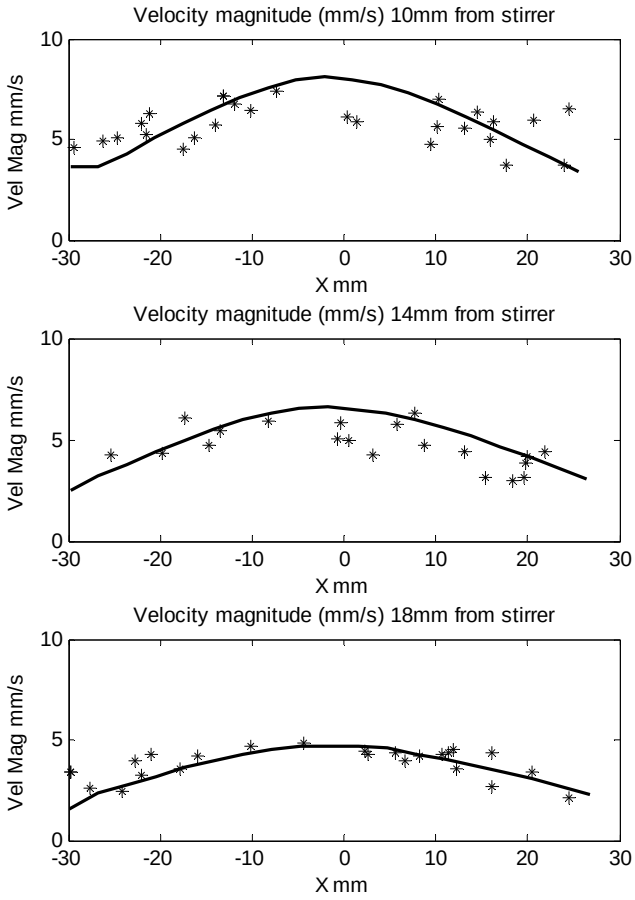

a) Velocity magnitude comparison

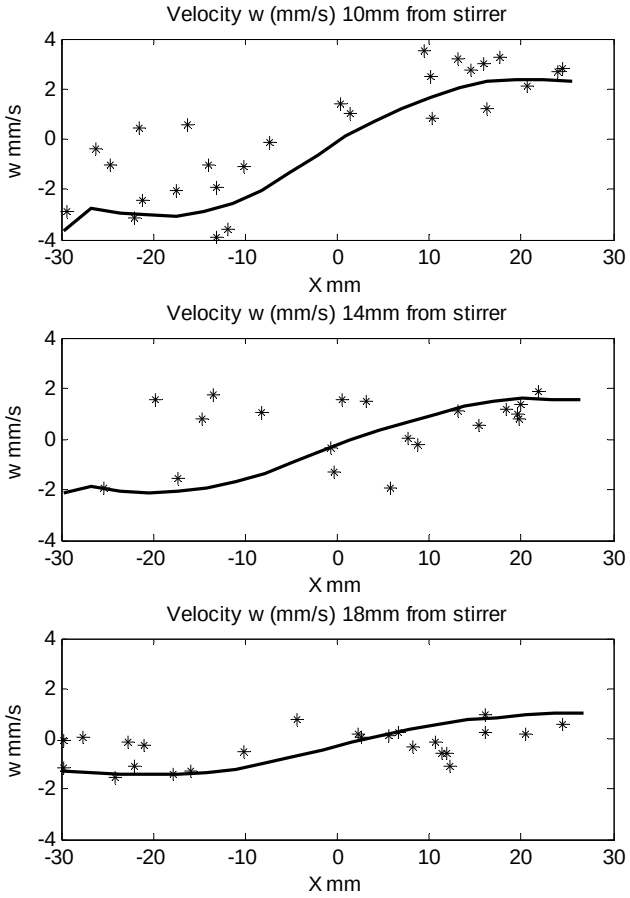

b) w component velocity comparison

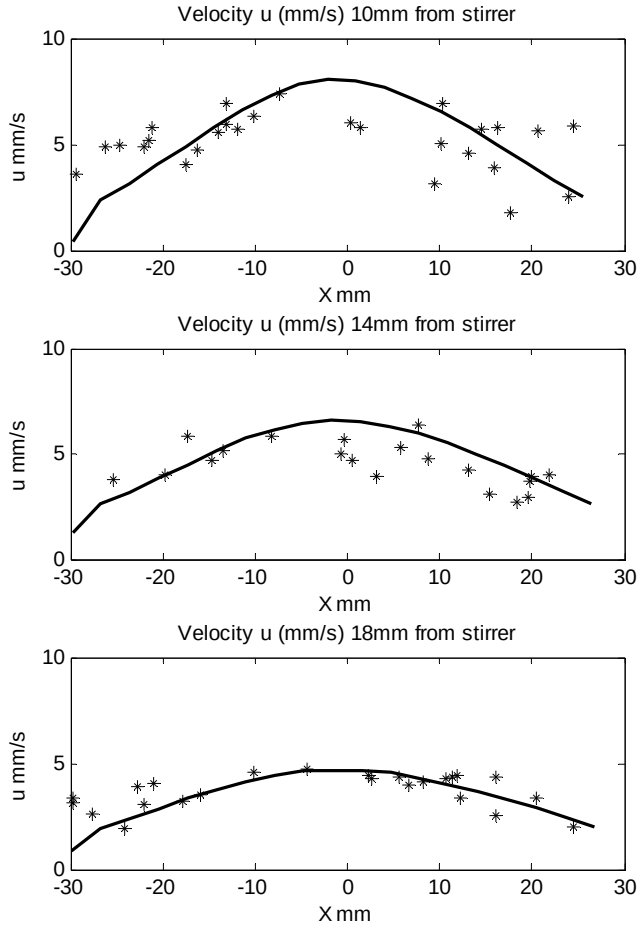

c) u component velocity comparison

Figure 6.8. Comparison of velocities from 2D-PIV and 3D-PTV
Lines--Velocity distribution from 2D-PIV
Stars--Velocity of individual particles from 3D-PTV

Chapter 7

Application of 3D-PTV Technique to a Low Speed Stirred Tank

In this chapter, the 3D-PTV technique was applied to study the flow field generated by a rotating rectangular block in a viscous fluid. The setup simulates a stirred tank that could be used for mixing of pharmaceutical components. Measurements were taken at two different locations, with two different rotation speeds and with two different types of particles. The 3D particle trajectories, 3D velocity field, acceleration, and vorticity of the flow movement are analyzed and compared.

7.1 Background on Stirred Tank

Stirred tanks are widely used for mixing and blending of pharmaceutical ingredients. They are used to mix liquids, blend polymers, pastes and solids. Mixing at low Reynolds numbers tends to have lower efficiency and side reaction effects, and thus the understanding of the flow behaviors at low Reynolds numbers becomes more crucial [32].

Understanding the mixing in a stirring tank requires understanding the behavior of the different fluid constituents and their evolution as a function of time. The flow investigation can be done by either computational simulation or flow visualization experiments. Computational Fluid Dynamics (CFD) is the most common method used to study the flow field. Some research was also done with experimental methods. Guiraud et al. (1997) studied the turbulent mixing an industrial axial propeller in a fully baffled vessel, with the phase Doppler technique. The fluid was water and seeded with glass spheres at low concentration. A 2D vector field was obtained at the side of the stirrer [33]. A phase-locked stereoscopic PIV system was applied by Yoon et al. (2005) on three different vertical planes close to the impeller of a high Reynolds number stirred tank. 2D velocity fields were obtained [34]. Lamberto et al. (1999) used fluorescent dye and single PIV system to investigate the flow in an unbaffled stirred tank [35].

The research stated above all focused on the Eulerian description of the flow in stirred tanks. Lagrangian description with particle trajectories, however, is desired to better understand the mixing process especially for multiphase flows. Fangary et al. (2000) obtained particle trajectories by the technique of positron emission particle tracking (PEPT). They were able to obtain particle trajectories within a stirred vessel with axial impellers [36]. However, the system requires costly equipments like positron cameras and position-sensitive gamma-ray detector and the total number of trajectories is also restricted. A recent work by Guha et al. (2007) introduced another solution known as

computer automated radioactive particle tracking (CARPT) to study the solid suspension in a stirred tank reactor [37]. The CARPT system maps the solids motion by tracking single radioactive particles that are of same size and density as the actual solids. The system requires delicate calibration procedure and is of considerably complexity.

The approach presented here is the first to apply an optical flow measurement technique to track the evolution of individual particles in a stirred tank as a function of time to provide their Langrangian trajectories. Compared with PEPT and CAEPT techniques stated above, this optical flow diagnostic technique is less complex, less expensive and more robust and able to track a larger number of particles at any given time. Here, the 3D-PTV system is applied on the stirred tank and the real particles traces, as well as the velocity field, acceleration, and vorticities are obtained.

7.2 Description of the Stirred Tank

The measurements are performed inside a rectangular tank that contains a stirrer submerged in glycerin. A sketch of the setup is shown in Fig. 7.1. The stirrer is made of clear acrylic plastic with dimensions 51mm x 51mm x 23mm. Acrylic plastic was chosen as the material of the stirrer because its index of refraction (n=1.49) is very similar to that of glycerin (n=1.473). The stirrer had all the surfaces finely polished, and it optically disappears in the fluid. It was optically invisible since the index of refraction between the

stirrer and the glycerin are the same, which also greatly reduces any reflections produced by the stirrer when hit by the laser light. The stirrer was connected to a gear motor with rotation speed proportional to the voltage input. The gear motor is connected to a DC power supply with adjustable power output. The rotation speed of the gear motor output was calibrated with the voltage input at discrete points. The final experiments used two rotation speeds: 0.1revolution/s and 0.3revolution/s, which could be obtained with voltage input of 9.7 Volts and 26.5 Volts accordingly.

The Reynolds number for stirred tank is defined as: [35]

$$Re = \frac{\rho \times N_{rps} \times D^2}{\mu}, \tag{7.1}$$

where ρ is the density of the fluid, N_{rps} is the stirrer speed in revolution per second, D is the diameter of the stirrer, and μ is the kinematic viscosity of the fluid. The values for the experimental set-up parameters used are shown in Table 7.1. For this laminar flow, the Reynolds number calculated was 23.6 and 70.8.

Parameters	Diameter of Stirrer (D)	Rotation Speed of Stirrer (N_{rps})	Density of Fluid (ρ)	Kinematic Viscosity of Fluid (μ)
Values	51mm	0.1or 0.3 revolution/s	1259.37kg/m^3 @25°C	1.5Pa s @25°C

Table 7.1. Parameters for the stirred tank measurements

The tracer particles used in the experiments are aluminum oxide particles with diameters of 150 microns and 500 microns. The seeding concentration of the particles was

approximately 6 particles/cc. This concentration provided a particle distribution of about 1000 particles in each PTV image.

Fig. 7.1 shows the location of the stirrer. Measurements were done at two different locations: 10mm and 30mm from the stirrer axis. The dimensions and vertical locations of the two observation volumes were the same. Both locations are on the side of the stirrer as shown in Fig. 7.2. Since the motion of the stirrer is axisymmetric, taking data on one side is enough to describe the motion around the stirrer.

7.3 Results of Stirred Tank Experiments

Nine cases, which are listed in Table 7.2, were considered using the stirred tank set-up. 3D PTV results were obtained for all of them. All the cases were analyzed and the percentages of particle correspondence for these cases are given in Table 7.3. The velocity at the edge of the stirrer was calculated as follows:

$$V_{edge} = N_{rps} \times 2\pi(D/2). \quad \textbf{(7.2)}$$

For the fast and slow cases, the velocities of the stirrer's edge were 16 mm/s and 48 mm/s respectively. The frame rate of the camera was 15 frames/s. For this frame rate and stirrer velocity, the velocity displacements expected would be 15pixels/frame and 45pixels/frame. In other words, a particle would travel 15-45 pixels between frames. Those displacements seem very large for any practical particle tracking measurement.

However, as the viscosity of glycerin is high, the actual flow velocity decayed very quickly as it gets away from the stirrer. Measurements show that the 3D PTV system provided the best results for displacements of about 8 pixels/frame. For the near field measurements, the average movement of the flow/particles is faster than the 3D PTV ideal conditions of 8 pixels/frame. Thus the 15 frame/s system was not fast enough for the near field view of the fluid in fast stirrer speed. The decreasing percentage of links out of valid particles for case 7 and case 8 showed this. The statistics for the 9 cases are given in Table 7.2 &7.3.

Cases	Stirrer Rotation Speed (revolution/s)	CCD Capture Rate (frame/s)	Measurement Volume Location	Particle Size (microns)	Sequences
1	0.1	15	Far Field	150	75 x 24=1800 (75=1/2 revolution)
2	0.1	5	Far Field	150	100 x 5=500 (100=2 revolutions)
3	0.3	15	Far Field	150	50 x 10+100 x 5=1000 (50=1 revolution 100=2 revolutions)
4	0.3	15	Far Field	500	100 x 5=500 (100=2 revolutions)
5	0.1	5	Far Field	500	100 x 5=500 (100=2/3 revolution)
6	0.1	15	Near Field	150	75 x 24=1800 (75=1/2 revolution)
7	0.3	15	Near Field	150	100 x 10=1000 (100=2 revolutions)
8	0.3	15	Near Field	500	100 x 5=500 (100=2 revolutions)
9	0.1	15	Near Field	500	100 x 5=500 (100=2/3 revolution)

Table 7.2. Lists of cases taken for the stirred tank experiment

		Fast Rotation		Slow Rotation	
Small Particles	Far Field	Case 3		Case 1	
		Quadruplets/All valid Particles	32%	Quadruplets/All valid Particles	39%
		Links/Particles	48%	Links/Particles	44%
	Near Field	Case 7		Case 6	
		Quadruplets/All valid Particles	10%	Quadruplets/All valid Particles	20%
		Links/Particles	27%	Links/Particles	50%
Large Particles	Far Field	Case 4		Case 5	
		Quadruplets/All valid Particles	33%	Quadruplets/All valid Particles	28%
		Links/Particles	43%	Links/Particles	49%
	Close Field	Case 8		Case 9	
		Quadruplets/All valid Particles	10%	Quadruplets/All valid Particles	33%
		Links/Particles	20%	Links/Particles	53%

Table 7.3. Statistic test results for different cases

7.3.1 Results at Different Locations

Cases with the same particle size (150 microns), same rotation speed (0.1 revolution/s), but different observation volumes are compared below. As shown in Fig. 7.3, the 3D trajectories of the particles are presented for 50 time steps. The shorter trajectories for the far field indicate the slower velocity with the observation volume moving away from the stirrer. Fig. 7.4 shows the trajectories in the XZ plane. The two observation volumes are overlapped for 20 mm along the z direction. From the top view, similar trajectories can be found within the overlapped areas, which validate the coherency of the system.

7.3.2 Results at Different Rotation Speeds

Cases with the same particle size (150microns), same observation volume (far field), but different rotation speeds are compared next. Fig 7.5 gives the 3D trajectories of the particles within 50 time steps. With the rotation speeds three times different from each other, the flow didn't move correspondingly with three-time different speeds. It is also noted that with faster rotation speed, the particle velocity in vertical direction caused by gravity difference is reduced. From Fig 7.6, the XZ view of the trajectories shows that the slow rotation speed creates more 'curly' trajectories which may be due to the high viscosity of glycerin.

7.3.3 Results with Different Particle Size

Cases with the same rotation speed (0.1revolustion/s), same observation volume (near field), but different particles are compared next. As shown in Fig. 7.7, the trajectories of the large particles have a sinking tendency. The 500micron particles do not follow the flow very well and are subjected to larger gravity difference. At this point, the case can be considered as two-phase flows with solid phase in viscous fluid. Fig. 7.8 indicate that the large particle do not rotate as much as the small ones and have more 'straight' trajectories.

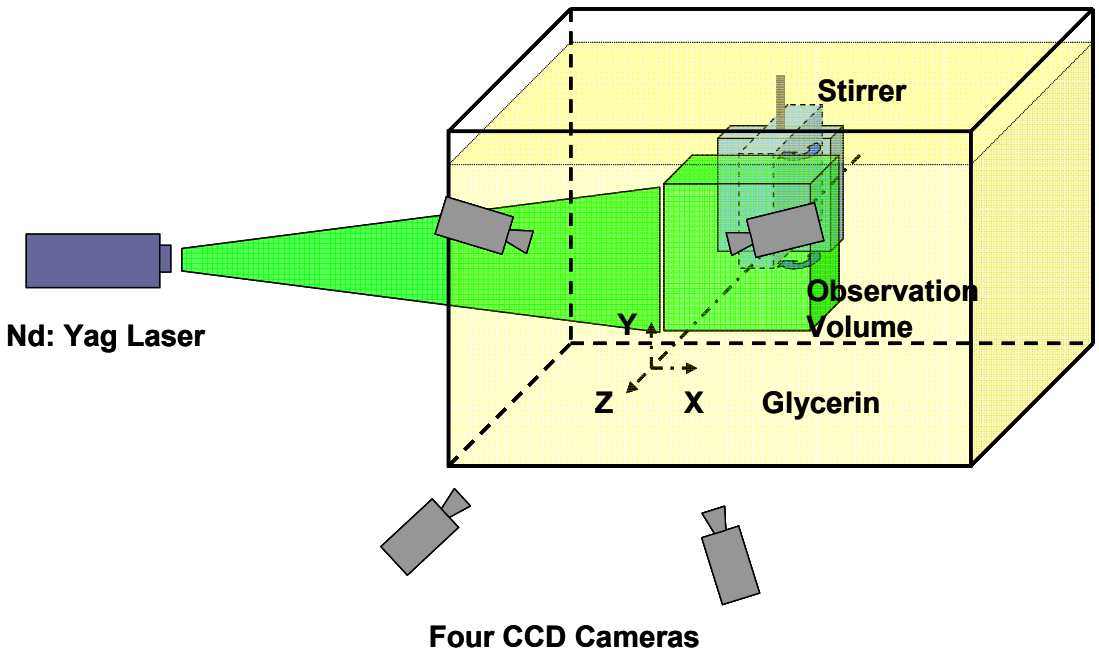

Figure 7.1. Experimental setup showing the 3D-PTV measurement system and the stirred tank

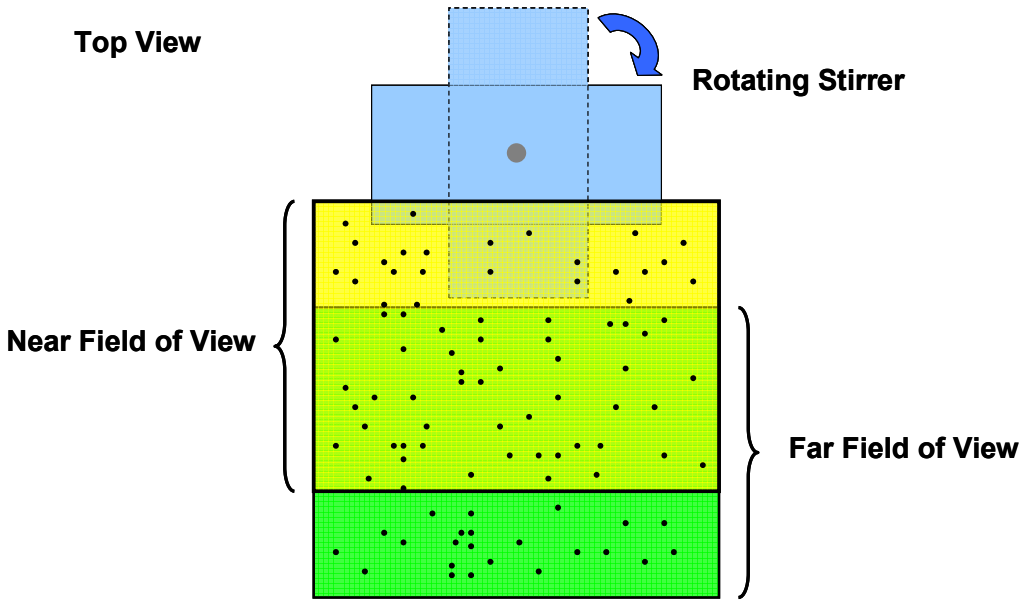

Figure 7.2. Sketch showing the position of the observation volume with respect to the rotating stirrer for the two cases considered (near field and far field)

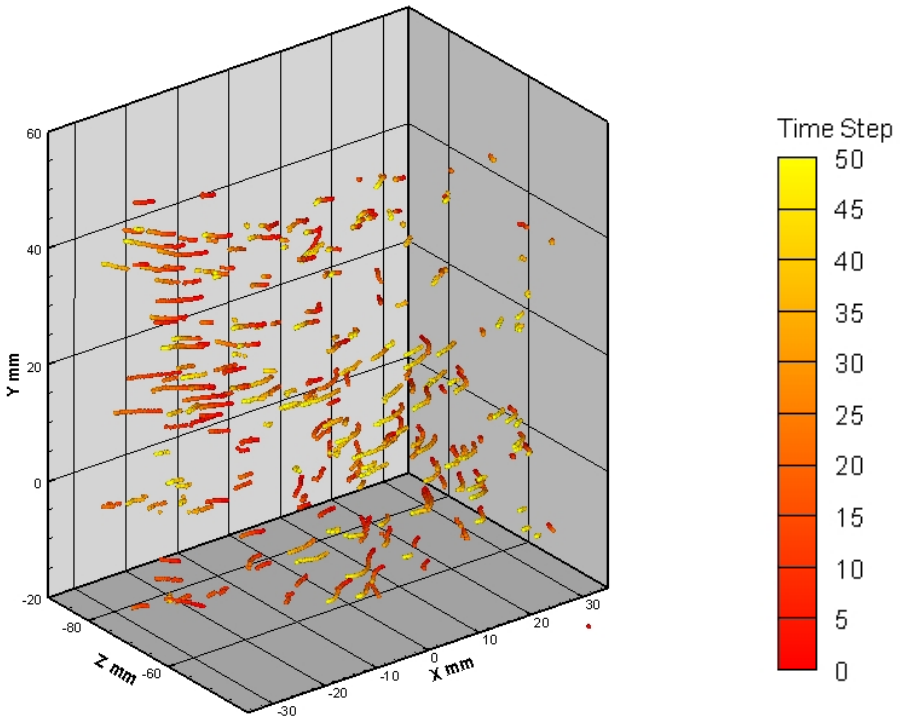

a) Near field -- Case 6

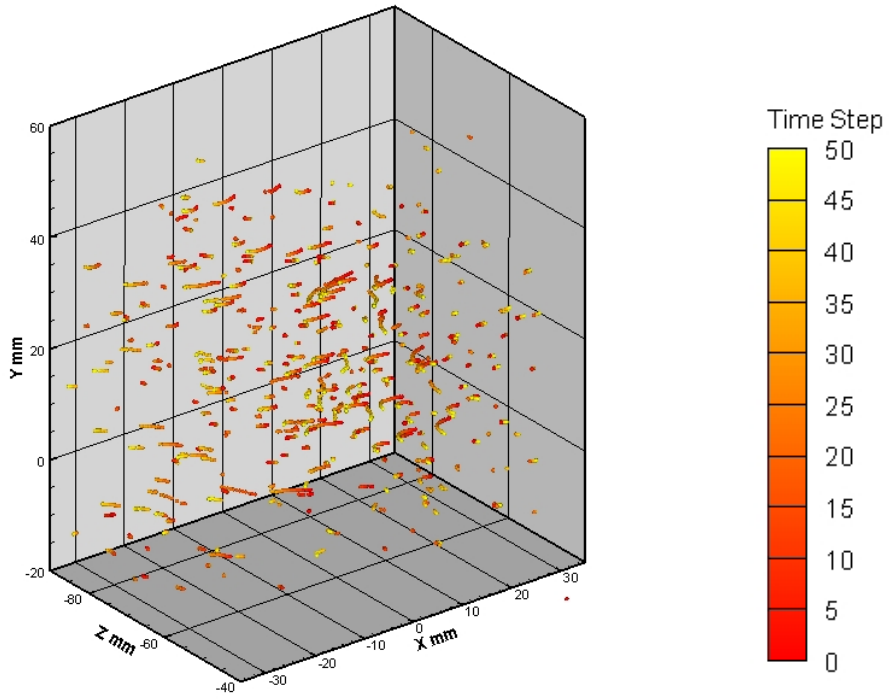

b) Far field -- Case 1

Figure 7.3. 3D trajectory comparison at different locations
a) Near field; b) Far field
Both taken at slow rotation speed (0.1revolution/s) with small particles (150microns)

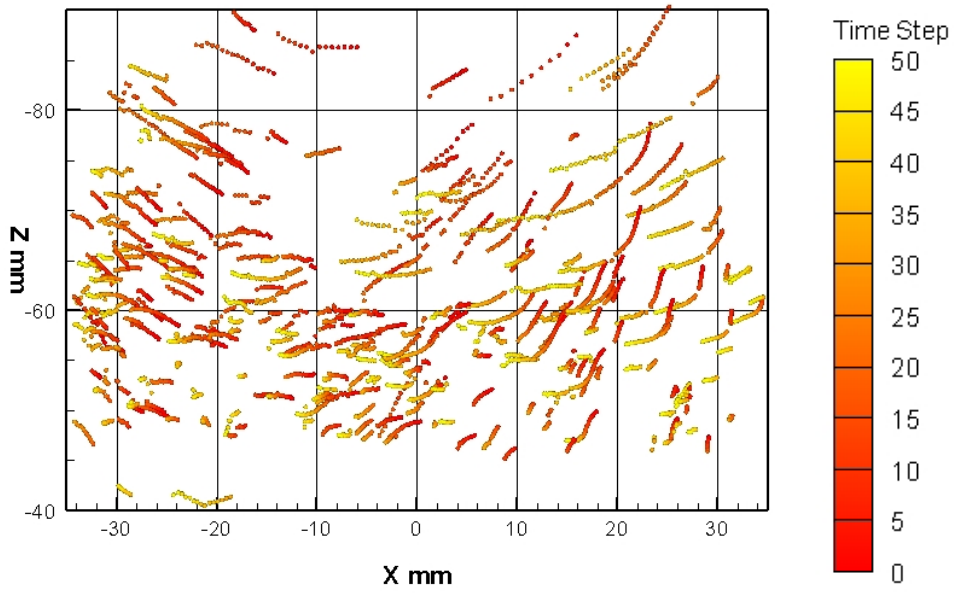

a) Near field -- Case 6

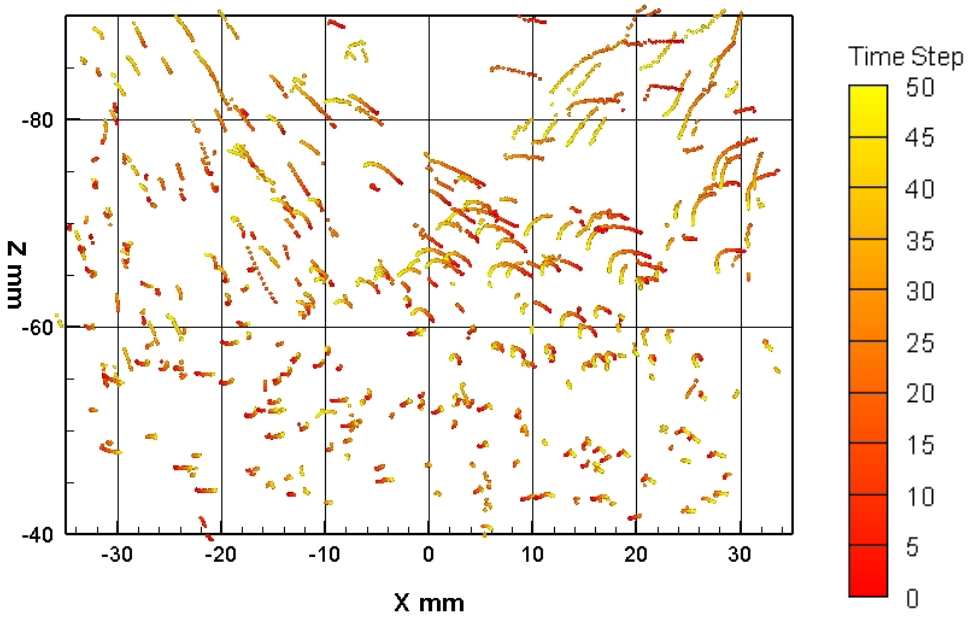

b) Far field -- Case 1

Figure 7.4. Top view (XZ plane) of trajectory comparison at different locations
a) Near field; b) Far field
Both taken at slow rotation speed (0.1revolution/s) with small particles (150microns)

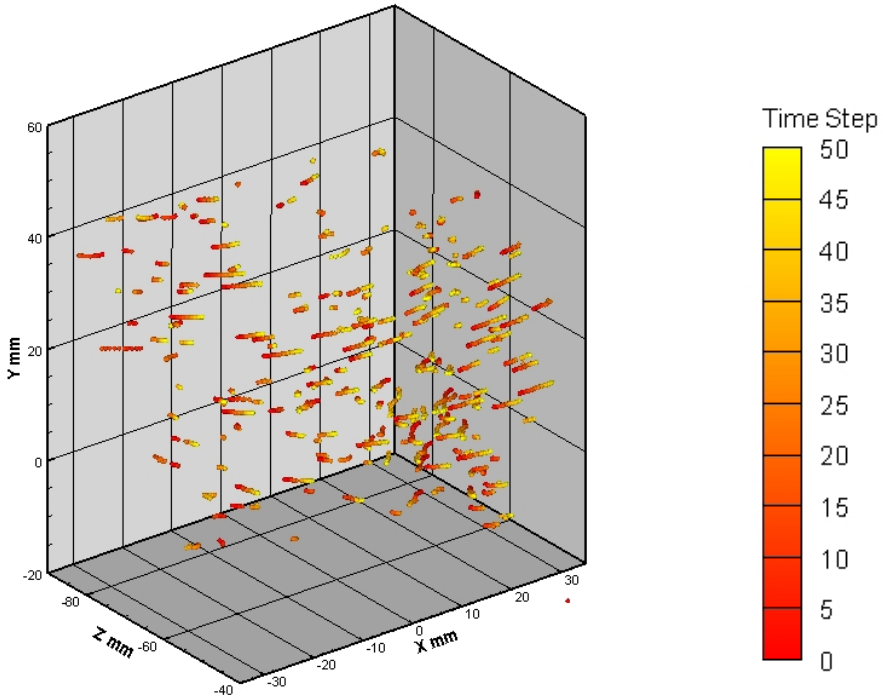

a) Fast speed (0.3revolution/s) -- Case 3

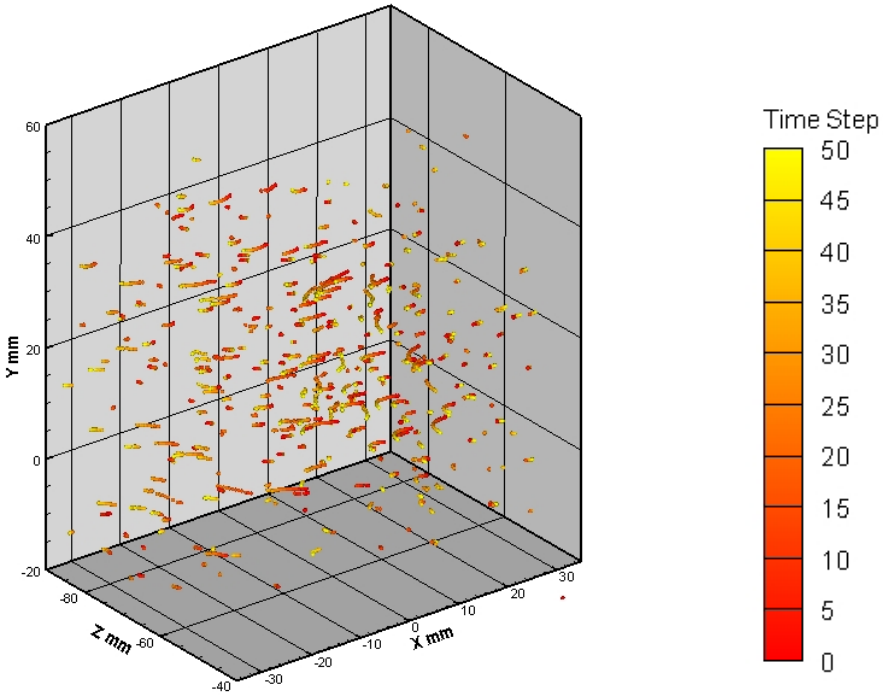

b) Slow speed (0.1revolution/s) -- Case 1

Figure 7.5. 3D trajectory comparison of different rotation speeds
a) Fast speed (0.3revolution/s); b) Slow speed (0.1revolution/s)
Both taken at far field with small particles (150microns)

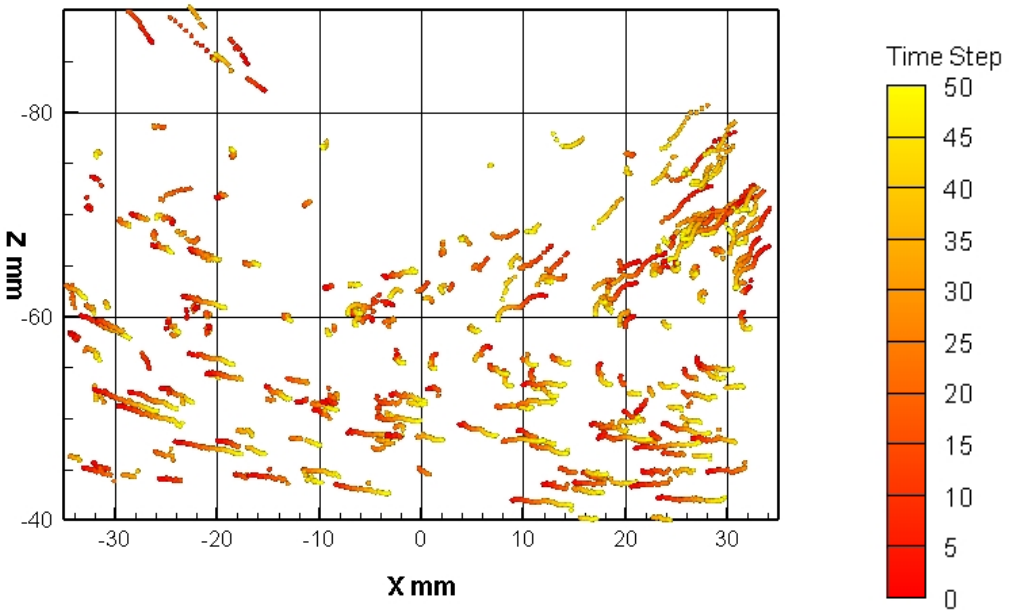

a) Fast speed (0.3revolution/s) -- Case 3

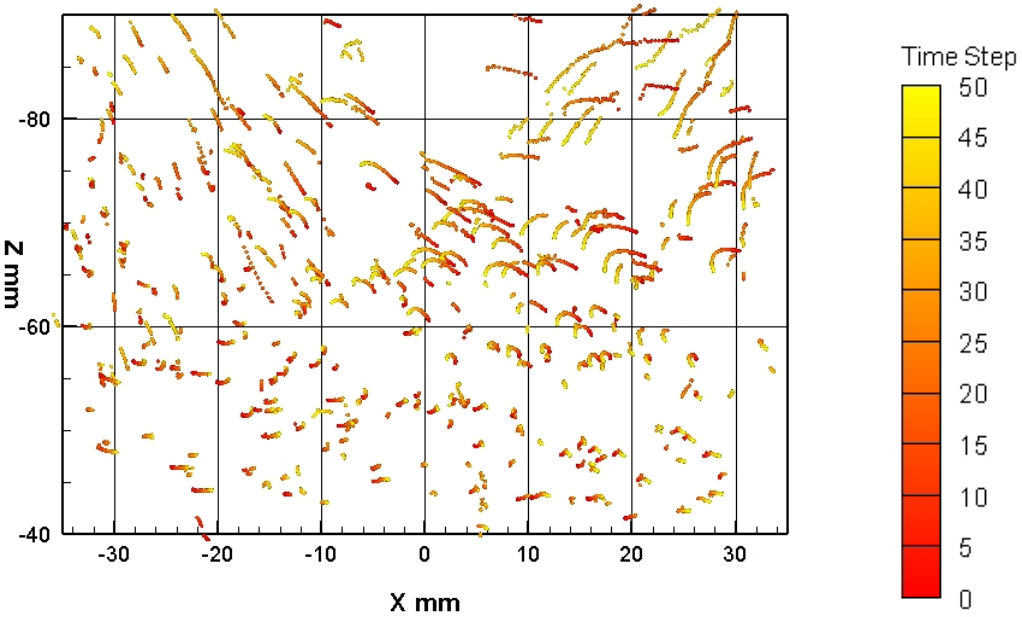

b) Slow speed (0.1revolution/s) -- Case 1

Figure 7.6. Top view (XZ plane) of comparison of different rotation speeds
a) Fast speed (0.3revolution/s); b) Slow speed (0.1revolution/s)
Both taken at far field with small particles (150microns)

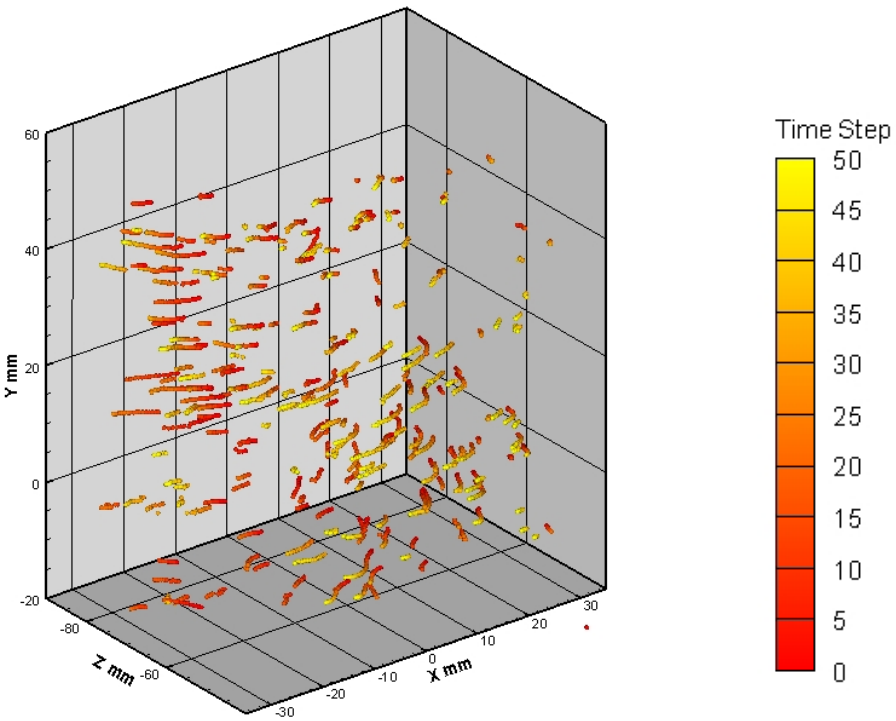

a) Small particles (150microns) -- Case 6

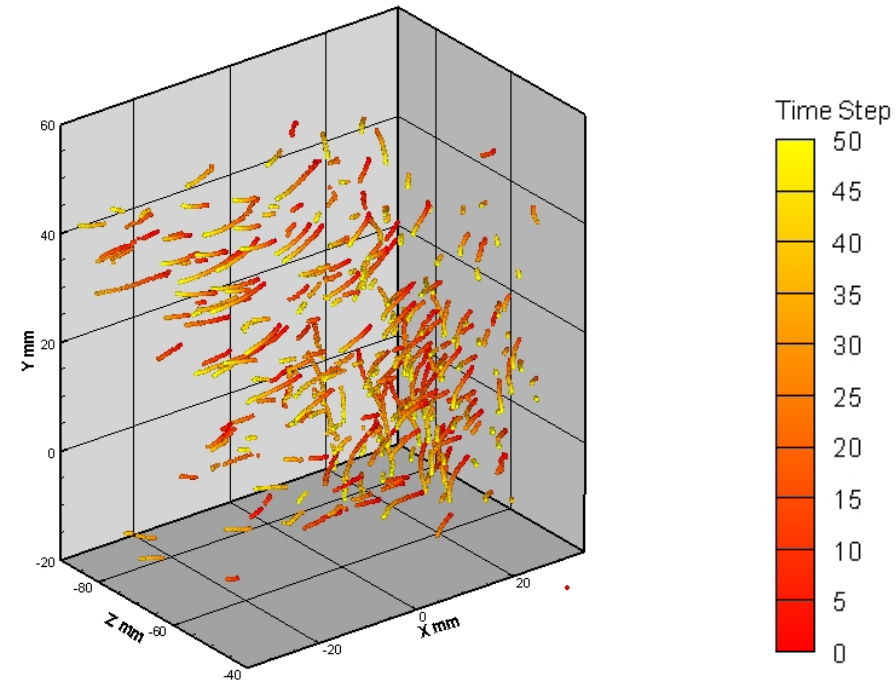

b) Big particles (500microns) -- Case 9

Figure 7.7. 3D trajectory comparison of different particle sizes
a) Small particles (150microns); b) Big particles (500microns)
Both taken at near field at slow rotation speed (0.1revolution/s)

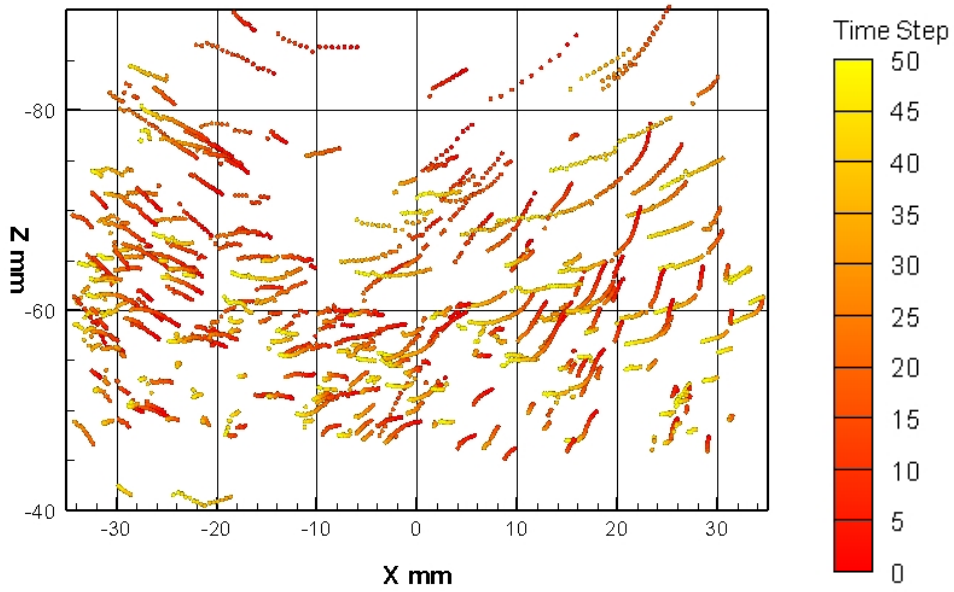

a) Small particles (150microns) -- Case 6

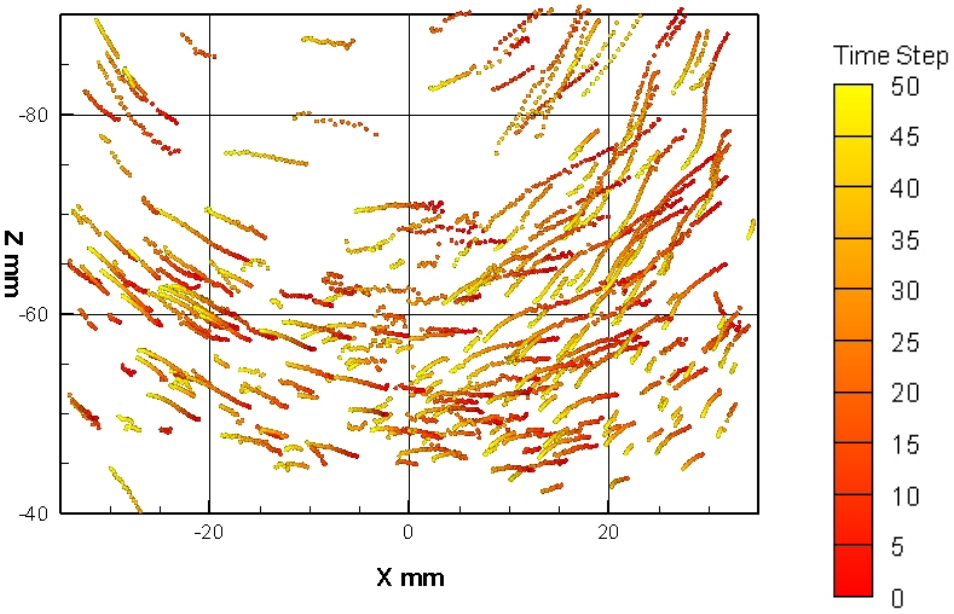

b) Big particles (500microns) -- Case 9

Figure 7.8. Top view (XZ plane) of trajectory comparison of different particle sizes
a) Small particles (150microns); b) Big particles (500microns)
Both taken at near field at slow rotation speed (0.1revolution/s)

Chapter 8

Concluding Remarks

This final chapter gives the concluding remarks of this work on the development, verification, and application of three-dimensional particle tracking velocimetry technique. Recommendations for future work are also presented.

8.1 Review of Results

8.1.1 The Influence of Different Components

One important part of this work was to study the influence of various hardware and software variables on the accuracy of 3D-PTV measurements. s. Results showed that the calibration target needs to have precisely shaped and located calibration dots of high contrast from the body, suitable dimensions for the object flow, and most importantly, appropriate spacing along all x, y and z directions to provide adequate calibration references. The creation of the laser light volume should always be based on the rule of

generating enough light intensity and corresponding to the field and depth of view of camera lens. Tracer particles should be chosen to match the gravity of the fluid, dynamically follow the flow, have appropriate size and even shape, and scatter enough light to be detected by the cameras. The accuracy of the system increases with the number of cameras, but not significant after the number reaches four. The orientation of the cameras needs to find a compromise between higher accuracy but poorer particle detection with larger viewing angles and better particle detection but lower accuracy with smaller viewing angles. A square camera configuration proved to have the better performance in terms of particle correspondence and accuracy.

8.1.2 Validation of the 3D-PTV Measurement system

Another important part of this work was to test and validate the 3D-PTV technique with a conventional 2D-PIV system. Both systems were tested under the same flow conditions. The velocity contour of the 2D-PIV taken at horizontal planes was compared with the horizontal view of 3D-PTV trajectories and their trends matched qualitatively. The 3D velocity of 3D-PTV was calculated from the particle positions at different time steps, and was then compared to the velocity gained from 2D-PIV measurements at different locations. The results showed good quantitative correspondence between the velocity information from the two methods.

8.1.3 Application of 3D-PTV system to mixing in a stirred tank

The 3D-PTV system was applied to the study of low Reynolds number mixing in a stirred tank. Different impeller rotation speed, different observing locations, and different particle sizes were tested with the system. The system was able to provide individual particle Lagrangian trajectories in a considerably large volume over long time intervals, particle velocity distribution and 3D velocity profiles in a volume. This is the first time that this Lagrangian approach has been applied to flow measurements in stirred tank.

8.2 Conclusion of This Work

This work is based on the 3D-PTV system developed at the Institute of Geodesy and Photogrammetric at the Swiss Federal Institute of Technology, Zurich. The theoretical principles were studied based on geometric imaging and computer vision. The 3D-PTV system was designed, assembled, synchronized, and tested while giving careful consideration to the influence of each element to the accuracy of the measurements. A conventional 2D-PIV system was set up to validate the measurements of the 3D-PTV system. The developed 3D PTV system was applied to the study of mixing in a stirred tank showing that this technique has great potential for the study of low Reynolds number flows where the time-resolved trajectory of particles is important

8.3 Future Work

Recommendations for future work include extending the capabilities and accuracy of the 3D PTV measurement system. This includes: (1) the use of smaller particles, that can be consider passive tracers; (2) improving the accuracy of the reconstruction algorithms to increase not only the number of particle correspondence, but also the seeding concentration; (3) extend the system to study higher speed flows by using high speed cameras (i.e.: 1000 fps) and, with small size particles. In terms of system configuration, with the rapid development of science and technology on photography, laser optics, data acquisition, computer, etc., the spatial and temporal resolution and the accuracy of the system can be expected to improve over time. The 3D-PTV system can also be combined with PIV system for better spatial resolution or extended application on multiphase flows.

References

[1] M. Raffel, C. Willert, and J. Kompenhans (1998) Particle Image Velocimetry-A Pratical Guide. Springer, Berlin Heidelberg New York.
[2] M. Gaydon, M. Raffel, C. Willert, M. Rosengarten and J. Kompenhans (1997) Hybrid stereoscopic particle image velocimetry. Exp. Fluids, 23, pp. 331-334.
[3] R. J. Adrian (2005) Twenty years of particle image velocimetry. Exp. Fluids, 39, pp. 159-169.
[4] S. Soloff, R. J. Adrian, and Z. C. Liu (1997) Distortion compensation for generalized stereoscopic particle image velocimetry. Meas Sci Technol, 8, pp. 1441-1454.
[5] M. Raffel, J. Westerweel, C. Willert, M. Gharib, and J. Kompenhans (1996) Analytical and experimental investigations of dual-plane particle image velocimetry. Optical Engineering, 35, pp. 2067-2074.
[6] O. Pust (2003) Time resolved PIV solutions-PIV at 4000 frames per second. The 12th International Conference on Fluid Flow Technologies, Budapest, Hungary.
[7] M. P. Wernet (2007) Time resolved PIV for space-time correlations in hot jets. 45th AIAA Aerospace Sciences Meeting and Exhibit, Reno, Nevada.
[8] Y. G. Guezennec, Y. Zhao, and T. J. Gieseke (1994) High-speed 3-D scanning particle image velocimetry (3-D SPIV) technique. Proceedings of the 7th International Symposium, Lisbon, Portugal, pp. 392-407.
[9] M. Ciofalo, M. Signorino, and M. Simiano (2003) Tomographic particle-image velocimetry and thermography in Rayleigh-Benard convection using suspended thermochromic liquid crystals and digital image processing. Exp. Fluids, 34, pp. 156-172.
[10] R. Hain, C. J. Kähler, and D. Michaelis (2008) Tomographic and time resolved PIV measurements on a finite cylinder mounted on a flat plate. Exp Fluids, 45, pp. 715-724.
[11] T. Hori and J. Sakakibara (2004) High-speed scanning stereoscopic PIV for 3D vorticity measurement in liquids. Meas. Sci. Technol., 15, pp. 1067-1078.
[12] D. H. Barnhart, R. J. Adrian, C. D. Meinhart, and G. C. Papen (1994) Phase-conjugate holographic system for high-resolution particle image velocimetry. Applied Optics, 33, pp. 7159-7169.
[13] H. Meng and F. Hussain (1995) In-line recording and off-axis viewing technique for holographic particle velocimetry. Appl. Opt., 34, pp. 1827-1840.
[14] J. Sheng, E. Malkiel and J. Katz (2003) Single beam-two views holographic particle image velocimetry system. Appl. Opt., 42, pp. 235-250.
[15] Y. A. Hassan and R. E. Canaan (1991) Full-field bubbly flow velocity measurements using a multiframe particle tracking technique. Exp. Fluids, 12, pp. 49-60.
[16] G. Labonté (1999) A new neural network for particle-tracking velocimetry. Exp. Fluids, 26, pp. 340-346.
[17] D. Papantoniou and H. G. Maas (1990) Recent advances in 3-D particle tracking velocimetry. Proceedings 5th International Symposium on the Application of Laser

Techniques in Fluid Mechanics, Lisbon.
[18] H. G. Maas, A. Gruen, and D. Papantoniou (1993) Particle tracking velocimetry in three-dimensional flows: Part 1. Photogrammetric determination of particle coordinates. Exp. Fluids, 15, pp. 133-146.
[19] N. Malik, T. Dracos, and D. Papantoniou (1993) Particle tracking velocimetry in three-dimensional flows: Part 2. Particle Tracking. Exp. Fluids, 15, pp. 279-294.
[20] H. G. Maas and A. Gruen (1995) Digital photogrammetric techniques for high-resolution three-dimensional flow velocity measurements. Optical Engineering, 34 No. 7.
[21] C. E. Willert and M. Gharib (1992) Three-dimensional particle imaging with a single camera. Exp. Fluids, 12, pp. 353-358.
[22] F. Pereira, M. Gharib, D. Dabiri, D. Modarress (2000) Defocusing digital particle image velocimetry: a 3-component 3-dimensional DPIV measurement technique. Application to bubbly flows. Exp. Fluids, 29, S78-S84.
[23] F. M. White (1986) Fluid mechanics, 2nd Edition. McGraw-Hill, Inc.
[24] M. C. Potter, and D. C. Wiggert (2001) Mechanics of fluids, 3rd Edition. Cengage-Engineering.
[25] V. S. Nalwa (1993) A guided tour of computer vision. Addison-Wesley Publishing Company.
[26] J. Willneff (2003) A Spatio-Temporal Matching Algorithm for 3D Particle Tracking Velocimetry. Ph.D. Dissertation, ETH, Zurich.
[27] R. J. Schalkoff (1989) Digital image processing and computer vision. John Wiley & Sons, Inc.
[28] E. R. Davies (2005) Machine vision, theory, algorithms, practicalities, 3rd Edition. Elsevier.
[29] H. G. Maas (1992) Complexity analysis for the establishment of image correspondences of dense spatial target fields. International Archives of Photogrammetry and Remote Sensing, XXIX, Part B5, pp. 102-107.
[30] Scanning Electron Micrograph of AG-SL150-16-TRD, Product Manual, Potters Industries INC.
[31] Y. Cheng, P. Vanderwerker, F. J. Diez, and D. Troolin (2007) Velocity discrimination algorithm of two-phase flows for time resolved stereo PIV. 7th International Symposium on Particle Image Velocimetry, Rome, Italy.
[32] D. J. Lamberto, F. J. Muzzio, P. D. Swanson, and A. L. Tonkovich (1996) Using time-dependent RPM to enhance mixing in stirred vessels. Chem. Eng Sci., 51, pp. 733-741.
[33] P. Guiraud, J. Costes, and J. Bertrand (1997) Local measurements of fluid and particle velocities in a stirred suspension. Chemical Engineering Journal, 68, pp. 75-86.
[34] H. S. Yoon, D. F. Hill, S. Balachandarc, R. J. Adrian, and M. Y. Ha (2005) Reynolds number scaling of flow in a Rushton turbine stirred tank. Part I—Mean flow, circular jet and tip vortex scaling. Chemical Engineering Science, 60, pp. 3169-3183.

[35] D. J. Lamberto, M. M. Alvarez, and F. J. Muzzio (1999) Experimental and computational investigation of the laminar flow structure in a stirred tank. Chemical Engineering Science, 54, pp. 919-942.
[36] Y. S. Fangary, M. Barigou, J. P. K. Seville, and D. J. Parker (2000) Fluid trajectories in a stirred vessel of non-newtonian liquid using positron emission particle tracking. Chemical Engineering Science, 55, pp. 5969-5979.
[37] D. Guha, P. A. Ramachandran, and M. P. Dudukovic (2007) Flow field of suspended solids in a stirred tank reactor by Lagrangian tracking. Chemical Engineering Science, 62, pp. 6143-6154.